NEAR-FIELD WIRELESS POWER TRANSFER AND COMMUNICATION SYSTEM DESIGN FOR CORNEAL INTRAOCULAR PROSTHETIC DEVICE

BY

SARAH YOONJI SHIM

THESIS

Submitted in partial fulfillment of the requirements
for the degree of Master of Science in Electrical and Computer Engineering
in the Graduate College of the
The University of Illinois at Urbana-Champaign, 2018

Urbana, Illinois

Adviser:

Assistant Professor Songbin Gong

Abstract

This thesis reports the design of a novel intraocular projection device for the treatment of intractable corneal opacity, with a design emphasis on the simultaneous wireless power and data transfer system. Electronic ocular prosthetics (EOP) or artificial eyes are devices designed to deliver artificial visual stimuli to patients with blindness to partially restore their visual function.

The need for wireless capabilities in EOPs arises from the highly limited physical space available for the intraocular implant devices. Early attempts at EOPs incorporated prohibitively large battery power sources and physical wire connections for the transmission of both power and information. However, one of the vital health regulations on medical implant devices involves the potential infection and inflammation caused by the implantation. Such regulations strictly prohibit the use of physical wire between the interbody and external-body components. This thesis presents a wireless power transfer (WPT) implementation that allows the battery to be kept outside of the patient's body, significantly reducing the size of the implanted components, while still supplying energy to the implant without a signal exchange wire. The designed devices maintain the needed power and data exchange with the embedded parts while minimizing potential health complications from surgically inserted cables and bulky embedded hardware.

Acknowledgments

First and foremost, I would like to sincerely thank my advisor, Professor Songbin Gong, for his support and mentorship throughout my graduate studies. He has shown extraordinary generosity and patience with me throughout my research. This thesis could not have been completed without his full support, and I am forever grateful for his wisdom, motivation, and advice that has shaped me in all aspects of my life. In addition, I would like to thank Professor Charles Yu of Stanford University and Professor Mark Rosenblatt of the University of Illinois at Chicago for their generous support of the project throughout the years. I learned so much from Professor Yu and I always respect his new ideas and his passion for the project.

It is my fortune to gratefully acknowledge the support of my friends and group members, Anming Gao, Liuqing Gao, Ruochen Lu, Yansong Yang, Arunita Kar, Brandon Arakawa, Ali Kourani, Ahmed Emad, Ali Lavasani, Dr. Ming-Huang Li, and Dr. Meisam Bahadori, for their support and generous care throughout my time in graduate school. I will never forget all the wonderful memories we made.

I am also thankful to the University of Illinois at Urbana-Champaign for giving me the opportunity to learn and grow as an engineer at one of the greatest institutions in the world. Special thanks to Jen Carlson for being so patient and helping me with so many things from classes to graduate assistantships. I am also extremely grateful to Jamie Hutchinson of ECE Editorial Services for his editorial support and guidance of my thesis.

I would like to thank my family: my parents, my brother, and my puppy, Gummy, for being my #1 cheerleaders.

Last but not least, I would like to thank my amazing best friend/boyfriend, Michael Breen, for his continued and unfailing love and support that made the completion of the thesis possible. I greatly value his contribution and am deeply grateful for his belief in me.

I consider myself the luckiest person in the world to have such loving and supportive friends, family, and co-workers standing beside me. My sincere thanks and gratitude to everyone who supported me throughout my graduate studies. This thesis would not have been possible without any one of you.

Contents

Chapter 1: Introduction

Wireless communication technology refers to the transmission of an electromagnetic signal between two or more apparatuses without the use of physical wires. The ability to communicate and transmit information without the hassle of physical wires has allowed numerous adaptations of wireless technology over a broad spectrum of applications, including telecommunication, defense, consumer technology, industrial technology, and healthcare. Recently, among these applications, the health industry has witnessed one of the most significant increases in the incorporation of wireless technology such as telemedicine, telehealth, clinical information systems, and electronic implant and prosthetic devices.

However, incorporating wireless technology capabilities to patient-care devices such as robotic prostheses and electronic implants presents complex and unique design challenges. For example, with in-body medical devices, the system should operate away from the body's resonant frequency to avoid a significant increase in the in-body power absorption. In addition, for smaller medical implants, the size of the antenna and the processor must be designed with a highly restricted form factor for the device to fit safely inside the body. Furthermore, all implant devices must undergo a thorough heat radiation assessment for any small amount of device heating may affect the body's internal fluid temperature and result in a dangerous health effect. Therefore, it is essential to understand and to design a high-performance system that conforms to these strict restrictions and limitations of patient-care devices.

This thesis investigates the design of a millimeter-scale wireless implant prosthesis for the most sensitive and the most critical sensory organ of the human body, the eye [1]. This chapter will introduce the subject with a brief history of the fundamentals of wireless technology followed by an overview of the concept, and the significance of near-field WPT technology in biomedical devices. Afterward, the chapter will present the motivation and the scope of research of the thesis.

1.1 History and Overview of WPT Technology

During the last century, a series of consecutive historical discoveries and new social trends fostered great momentum in the advancement of wireless power transfer (WPT) technology. While WPT

capabilities are readily found in today's modern society, from electric toothbrushes to 5G smartphones, the origin of the technology traces back to the 1820s. In April of 1820, during his lecture demonstration, Danish natural philosopher Hans Christian Oersted noticed that an electric current through a wire caused a compass needle nearby to deflect away from the magnetic north. After three months, Oersted published his results in a scientific pamphlet [2]. Though it was mainly qualitative and had no explanation, the publication caused an immediate sensation and fostered a new generation of research to discover the relationship between electricity and magnetism.

After the Oersted's discovery, a series of developments in the field of electricity and magnetism followed in evolutionary sequence. A month after Oersted's publication, French physicist Andre Ampere developed a quantitative explanation to describe the magnetic forces between current-carrying wires. A decade later, English scientist Michael Faraday discovered electromagnetic induction. Following these discoveries, in 1873, Scottish physicist James Maxwell published a compilation of a set of all-encompassing postulates that completed the understanding of electromagnetism (EM) as shown in the equations below:

$$\Phi_E = \oint_S \boldsymbol{E} \cdot d\boldsymbol{A} = \frac{q_{\text{enc}}}{\varepsilon_0} \quad \text{or} \quad \nabla \cdot \boldsymbol{E} = \frac{\rho}{\varepsilon_0} \tag{1.1}$$

$$\Phi_B = \oint_S \boldsymbol{B} \cdot d\boldsymbol{A} = 0 \quad \text{or} \quad \nabla \cdot \boldsymbol{B} = 0 \tag{1.2}$$

$$\oint_C \boldsymbol{E} \cdot d\boldsymbol{s} = -\frac{\partial}{\partial t}\int_S \boldsymbol{B} \cdot d\boldsymbol{A} \quad \text{or} \quad \nabla \times \boldsymbol{E} = -\frac{\partial \boldsymbol{B}}{\partial t} \tag{1.3}$$

$$\oint_C \boldsymbol{B} \cdot d\boldsymbol{s} = \mu_0\varepsilon_0 \frac{d}{dt}\int_S \boldsymbol{E} \cdot d\boldsymbol{A} + \mu_0 i_{enc} \quad \text{or} \quad \nabla \times \boldsymbol{B} = \mu_0\varepsilon_0 \frac{\partial \boldsymbol{E}}{\partial t} + \mu_0 \boldsymbol{j} \tag{1.4}$$

Solid understanding and development of EM led to the discovery of WPT research by Serbian-American engineer Nikola Tesla, who in 1891 created the first system that could wirelessly transmit electricity, the Tesla coil. In addition to his 278 patents and his discoveries of alternating current, tuned circuits, wireless power, and radio circuits, Tesla revolutionized the idea of inductive coupling between the driving and the working apparatus [3]. Tesla's discoveries and methods are still heavily utilized and adopted in designing wireless systems today, and an in-depth review of his research and accomplishments is found in [4].

Following many historical discoveries, considerable progress has been made in the development of high-efficiency WPT technology. Today, WPT is classified into two different categories, far-field and near-field transfer (Fig. 1.1). Although the boundaries between the two classes are not sharply defined, there are some distinctive characteristics. The far field link is a WPT in which the physical dimensions of the system are much larger than the wavelength of the carrier frequency, whereas a near-field coupling refers to the system in which the physical dimension is smaller than a wavelength at the carrier frequency. Because the signal must travel through a more extended range, far-field WPT often employs radiated/directive techniques such as microwave power transmission (MPT) or a LASER power transmission. Though a main advantage is its ability to travel a long distance, far-field WPT behaves very poorly in water-rich environments, such as underwater or in biological tissues. Through a fluid-filled medium, a far-field system experiences significant path loss due to its high power absorption characteristic in the medium [5], [6].

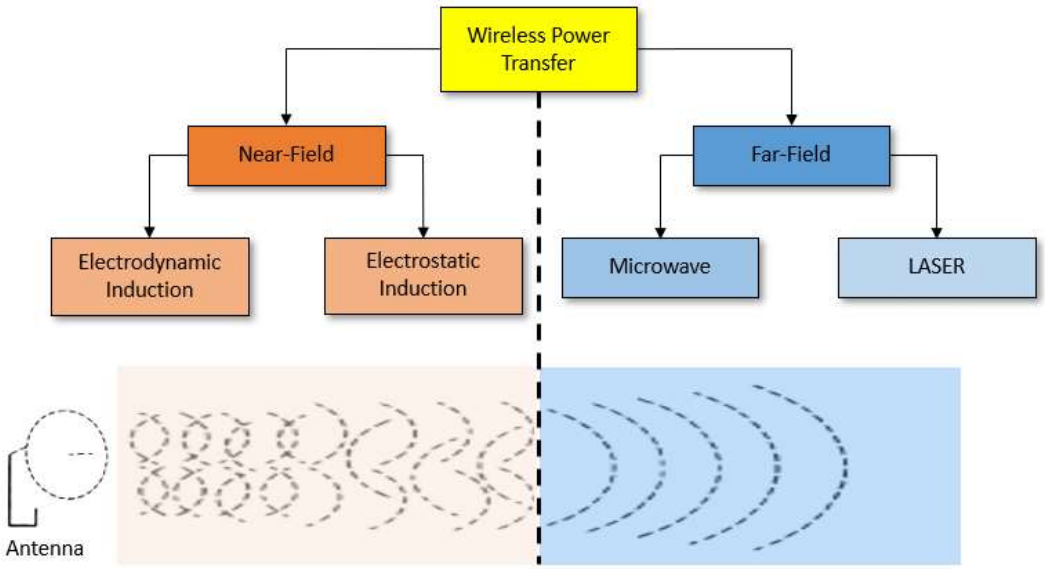

Figure 1.1. General diagram of the different types of WPT systems.

In contrast, the near-field WPT has a distinct advantage over the far-field when it comes to water-rich environments. Because the system experiences much less energy absorption in a lossy dielectric medium compared to its counterpart, the near-field magnetic systems are more efficient for medical device applications [6]. However, one disadvantage of using this type of system is that the power transfer efficiency (PTE) is very susceptible to change in the distance between the Tx and the Rx; the nature of the link requires that the Tx and Rx antennas be within each other's near-

field. The power densities decay at a rate of $1/r^3$ when the antennas are operating in the near-field compared to a rate of $1/r^2$ for far-field, where *r* is the operating distance (Fig. 1.2). This problem can be improved by using an optimal operating frequency and designing an effective matching network (which will be discussed in Chapter 4).

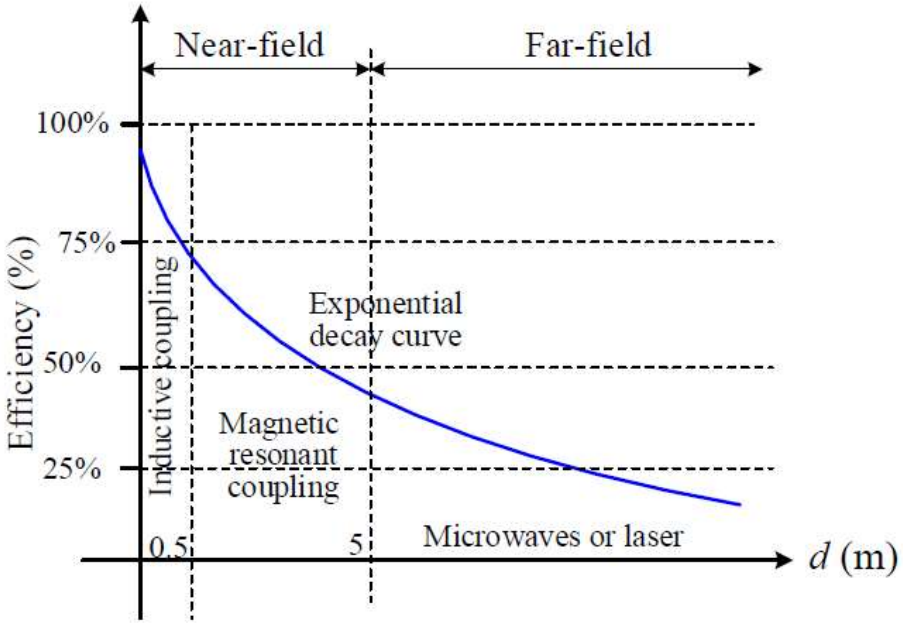

Figure 1.2. Comparison of efficiency for near-field vs. far-field WPT [7].

1.2 Motivation

As interest in wireless technology exploded, so did its use and the potential markets. Today, the wireless market size is estimated to be 69.44 billion USD and is expected to reach 116.75 billion USD by the year 2025 [8]. The largest market for wireless technology includes consumer technology and electronics (i.e., smartphones, computers, internet of things), industrial technology (i.e., aviation and construction), defense, and healthcare. According to the market report by Grand View Research, the next telecom and network infrastructure era is likely to spur immense growth in the healthcare sector, owing to the potential of high-quality data transmission and connectivity to enhance patient care and improve quality of life [8].

1.2.1 Robotic Prosthesis in Healthcare

The electronic implant device is one of the most extensive applications of wireless technology in healthcare. Recently, the modern healthcare industry has witnessed a significant increase in the global implantable prosthetics market. The key factors driving this market include a global rise in the number of patient cases, and increased initiatives taken by government organizations, such as the Center for Disease Control, and nonprofit organizations like the Amputee Coalition, to facilitate funding for and purchases of prosthetic devices. Moreover, the market has been significantly propelled by the U.S. government investing in technologically advanced prosthetic implants for soldiers and veterans. In addition, the growing usage and advancement of connectivity technologies such as wireless power transfer systems and information transmissions have resulted in increased demand for such devices.

Adopting wireless technology to implantable prostheses has been documented and published as early as 2000 [9]. Since then, many successful electronic implant devices have been invented, including the cochlear implant, cardiac pacemakers, cardioverter defibrillators, neuromuscular stimulators, and the artificial heart. However, unlike many other applications of WPT, there are specific challenges in designing a wireless system for electronic implants.

Currently, electronic implants, such as the artificial heart and the cochlear implant, rely heavily on batteries to power the devices. However, all batteries require maintenance and constant recharging, some more frequently than others. This makes the use of batteries impractical in the case of an implantable prosthesis since the device can only be accessed surgically. More importantly, the physical size of batteries adds a significant constraint to the highly limited design form factor of the device. This makes it impossible to design battery powered micro-scale implants. Furthermore, because all components of the implant must be kept entirely inside the body, physical wires cannot be used to connect internal and external-body components of the system. Therefore, a reliable wireless system will eliminate the problem of batteries and physical connectors and will significantly reduce the form factor limitation of microelectronic implants.

1.2.2 Robotic Prosthesis and Vision Rehabilitation

These design considerations are particularly important for ocular implants since the eyes are arguably the most critical and complex sensory organs in the human body. Recently, Zeiss has reported

that average humans perceive up to 80% of all impressions using their sight [10]. However, in 2012, the World Health Organization (WHO) announced that a population of 285 million people worldwide was reported to suffer from partial to extreme loss of vision [11].

Visual impairment, or blindness, can be classified into two major categories: internal and external. Internal impairment is caused by an injury or defect of the inner visual systems such as the retina (i.e., macular degeneration) and the optic nerve (i.e., glaucoma). In contrast, external impairment is caused by deterioration of the outer layers of the eye such as the cornea (i.e., corneal blindness) and the lens (i.e., cataract). According to WHO, corneal impairment is the number one leading cause of external blindness and the fourth leading cause of all blindness globally [12].

The cornea is the outermost, transparent surface of the eye [13]. However, due to its constant exposure to the external environment, the cornea is highly prone to injuries and infections. As seen in Fig. 1.3a, when it is injured from disease or dysfunction, the cornea becomes scarred, vascularized, and ultimately opaque, resulting in partial to complete blindness.

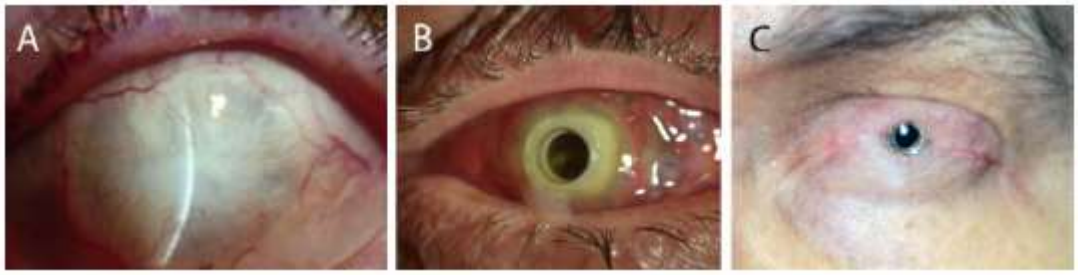

Figure 1.3. Human eyes under various conditions: (A) corneal scarring, (B) Boston Keratoprosthesis Type I with infection, (C) Type II Keratoprosthesis (Courtesy of Prof. Charles Yu from Stanford University).

A medical procedure called corneal transplantation is performed to replace the central area of an opacified cornea. However, the transplantation is only available in exceptional cases where the patient's cornea exhibits a complete absence of vascularization and has the surface stem cells fully intact [14]. In cases where the cornea displays vascularization, the transplanted cornea will directly be exposed to the host immune system and will result in transplantation rejection. Also, in cases where the surface stem cells are not intact on the cornea, the transplanted cornea will quickly opacify and will eventually fail. These conditions, medically termed high-risk cornea transplant, have resulted in a 50% failure rate of the operations performed in the last two years. In addition to

the problem of high-rate complication, there is a significant shortage of donated corneas worldwide, resulting in over 12.7 million patients currently on the cornea waitlists [14].

To address the problem of high-risk cornea transplant, researchers have developed corneal prosthetics in recent years. The most widely known of these prostheses is the Boston Keratoprosthesis Type I (K-Pro I). It is composed of two pieces of clear acrylic plates that are sandwiched between the patient's diseased cornea and is designed to remain clear even in the case of corneal rejection as shown in Fig 1.3b. Though the mechanism and the procedure of the K-Pro I sound simple and straightforward, the device has several critical limitations.

First, the success of the invention requires a continuous healthy material-to-tissue interface on the cornea. However, this interface is completely exposed to an external environment, and thus often results in a chronic risk of infection and a high rate of complication. Second, because the plates perturb the natural rigidity of the eye, it becomes difficult to make an accurate measurement of the patient's intraocular pressure and to detect any onset of severe internal conditions such as glaucoma, cataract, and age-related macular degeneration. Third, the cornea is one of the most innervated and sensitive parts of the human body. Surgically applying a foreign object to a cornea will significantly increase the chance of chronic inflammation of the eye. Recent studies have shown that K-Pro I patients are at high risk of membrane formation, extrusion, infection, and glaucoma, conditions that ultimately result in irreversible vision loss [15]. For these reasons, Keratoprosthesis is currently not considered as an appropriate first-line treatment for patients awaiting cornea transplant.

1.2.3 Electric Intraocular Implants and Visual Rehabilitation

To overcome the limitations of transplants and current prosthetics, there has been an increase in development of electronic intraocular implant (EII) prosthesis. EII refers to a millimeter scale electric device that is surgically implanted inside a damaged eye to artificially replace the impaired function(s) and enhance the patient's vision. One of the most recent and successful EII on the market is the Argus II electronic prosthesis (Fig. 1.4). This FDA approved device implants an array of electrodes directly onto the retina to artificially stimulate vision in patients who have retinal dystrophy. The device is secured in the posterior portion of the eye and receives power and data from an externally worn glasses apparatus. Figure 1.4 models and highlights the wearable external

unit and the implant apparatus of the device [16]. However, due to the nature of the retinal dystrophy disease and the placement of electrode array, the resolution of the Argus is strictly limited to 6 x 10 pixels.

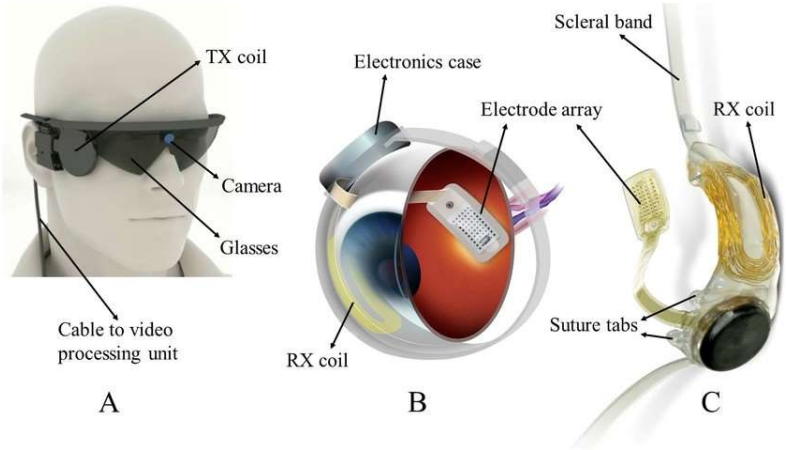

Figure 1.4. Argus II retinal prosthetics: (A) wearable external unit, (B) implant model, (C) retinal implant device c.

In addition to Argus, the Alpha IMS is a recently developed EII that has been approved for use in Europe. Even though the process and the targeted patients are similar as illustrated in Fig. 1.5 [17], unlike the Argus, this device have been successfully implanted sub-retinally with a light sensor and a 40x40 stimulator and connected to a retroauricular processor and power receiver coil using tunnel wires [17]. Though it has achieved greater resolution than the Argus, Alpha IMS also suffers from meager resolution compared to the resolution of 576 megapixels of a normal human eye.

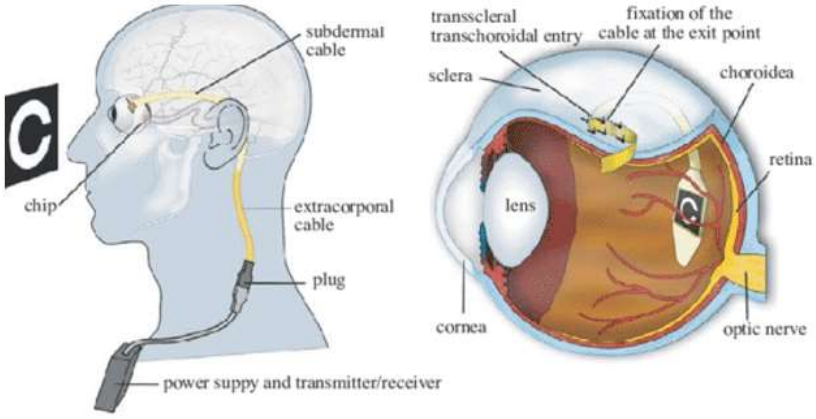

Figure 1.5. Alpha IMS retina stimulator, with tunneled cable and retroauricular wireless receiver.

However, unlike retinal dystrophy, in up to 80 percent of cases of the severe ocular surface disease, the interior contents of the eye remain intact [18]. Therefore, even though the frontal part of the eye may be damaged, the retina remains healthy and can detect high-resolution imagery with appropriate light input. This thesis presents an EII device that can project a focused image onto the retina and bypass an opacified cornea. If successful, the device can restore the vision of 256 x 144 pixels to patients which is at least six times the current resolution of the Alpha IMS.

1.2.4 Design of Corneal Intraocular Prosthetic Device

The thesis research proposes an EII device that offers an alternative to the Keratoprosthesis I and II by adopting approaches of the Argus II and the Alpha IMS. As shown in Fig. 1.6, by replacing the patient's crystalline lens with a microdisplay, the implant can directly stimulate the retina and create a clear artificial vision for the patient.

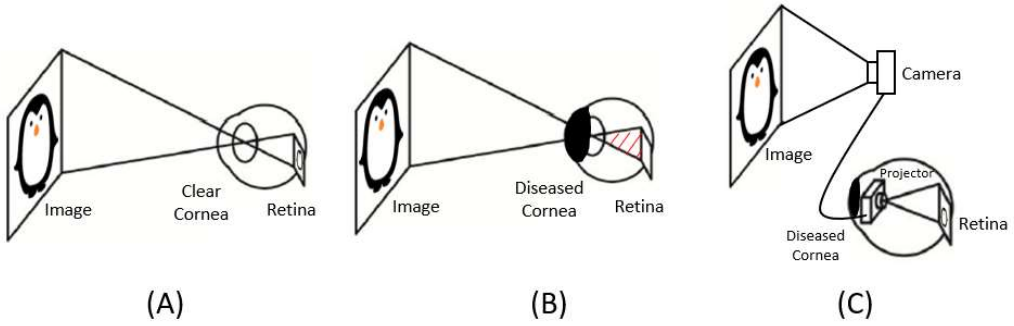

Figure 1.6. Comparison between the projection of image for a (A) healthy cornea, (B) diseased cornea, and the (C) proposed EII device.

As shown in Fig. 1.7, the proposed device is composed of two major components. The first part is an intraocular apparatus with fixation haptics that contains a liquid crystal microdisplay with associated light filters, and a focusing lens. The implant is waterproofed, sealed and fixated inside the anterior half of the eye. An extraocular unit that contains the electronics needed to make the display and backlight function, as well as a coil antenna to receive wireless power and video, is placed in the retroauricular region, and its wire tunneled subcutaneously to the eye (as with the Alpha IMS). The second part is the outer-body transmitter unit with a camera, processor, and transmitter coil to capture video imagery, process it and send it along with the power to the extraocular unit respectively.

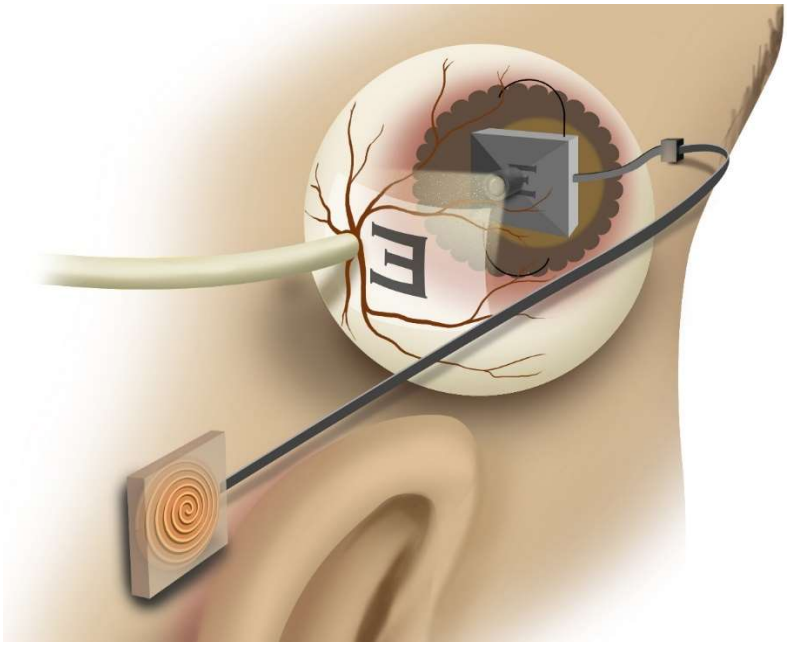

Figure 1.7. Interbody receiver unit of the proposed EII projector device.

1.3 Scope of Thesis

The rest of the thesis is organized as follows:

Chapter 2 focuses on the design choices of the wireless link of the device. Because a portion of the system will be implanted inside a human eye, there are several essential restrictions and concerns in designing the EOP device. This chapter takes an in-depth look at each of the significant limitations and forms design choices for a proposed wireless system.

Chapter 3 provides a viable system design following the design choices from the previous chapter and explains the choices for each of the system design components. Multiple generations of prototypes have been developed and presented as a proof of concept.

Design of a simultaneous power and data transfer system for the newest version of the prototype addressed in Chapter 3 is discussed and implemented in Chapter 4 and Chapter 5.

Finally, Chapter 6 discusses the result from the previous chapters, summarizes the material presented and discusses areas for future work.

Chapter 2: Design Choices

The human eye is an extremely robust optical instrument. In designing an intraocular projection device, it is essential first to understand the physiology and to appreciate how the eye processes the visual signal. In addition, when considering the design space of the implant, some of the important considerations include the limited physical space to fit the device and the highly sensitive nature of the organ. We will also investigate the limitations and range of acceptable parameters in this chapter.

2.1 The Eye and Visual Nervous System

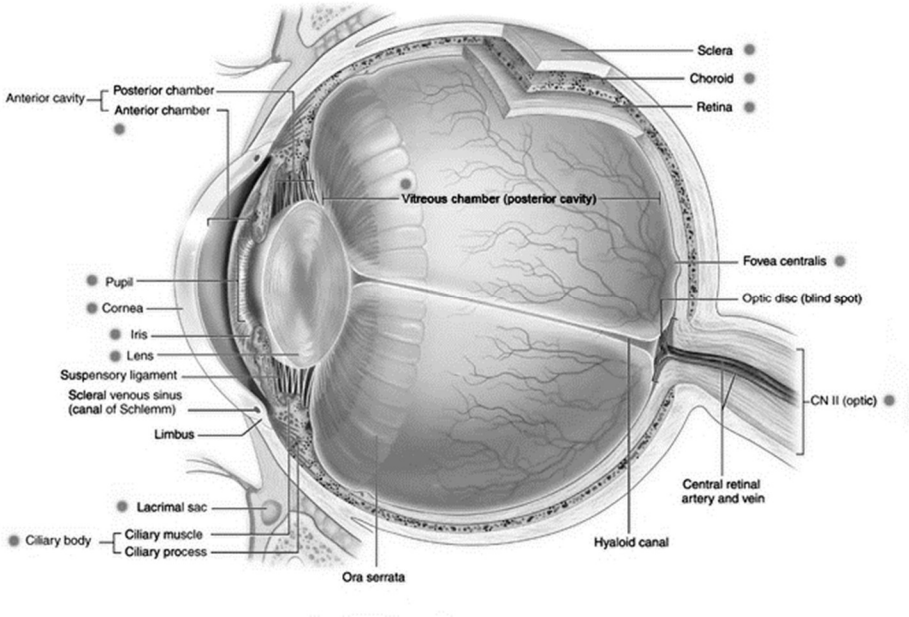

Figure 2.1. Basic anatomy of a human eye [19].

2.1.1 Anatomy and Physiology of Human Eye

The eye is a retinal-lined fibrovascular sphere of around 24mm in diameter that is divided into three regions. The basic anatomy of a human eye is illustrated in Fig. 2.1 [19]. The outer region includes the cornea and the sclera and is coated with tissues and cells to protect the eye [20]. The cornea is a transparent, protective window and the sclera is a white, opaque protective envelope of the eye.

Immediately internal to the outer region, the anterior layer of the eye is composed of the iris, the lens, and the ciliary body. The iris controls the size of the pupil and the amount of light that is

transmitting to the lens. The crystalline lens is the focusing mechanism of the eye and is located immediately anterior to the iris. The lens is supported by muscles in the ciliary body which controls its power and shape.

The innermost and arguably most essential part of the eye is the retina. The retina is a complex, multi-layered structure of neurons that capture and process the focused light from the lens. This part of the eye serves the primary purpose of photoreception and is an outlying island of the central nervous system [21]. Though much needed and crucial, all other structures of the eye are considered subsidiary to the retina [22].

2.1.2 Mechanism of Processing Vision

Sight is the most complex sense of the human body. Figure 2.2 illustrates the basic process of how an image is transferred onto the retina [21]. Sight works by projecting the incoming image onto the retina via two positive lenses: the cornea, and the crystalline lens [23]. The cornea first refracts the incoming light in the eye. The aqueous tear film on the cornea ensures that the optical surface is smooth to provide the best image quality. After the cornea, the image is sent through the pupil, the opening center of the iris. With two sets of muscles, the iris controls the amount of light passing into the pupil. The size of the aperture changes with the ambiance of the light, from less than 2 mm in diameter in bright light to more than 8 mm in the dark [24]. After the iris, the crystalline lens refracts the light signal to the fovea, where photoreceptors are densely packed to provide the highest resolution.

While the corneal lens has fixed optical power, the crystalline lens is an active optical element. Ligaments called zonules surround the crystalline lens, and these muscles control the magnitude of power. For the brain to create an image, the eye needs to convert light into electrical signals called the nerve impulses. This process is done in the retina, and the nerve impulses then are transmitted to the brain via the optic nerve.

The eyes move continuously to fixate the desired image onto the fovea, the central part of the retina. The peripheral portions of the retina, macula, render lower resolution but specialize in movement and object detection in the visual field. The typical field covered by the eye is about 160x130^{o} [23]. Figure 2.3 shows the general diagram of the visual system in the eye.

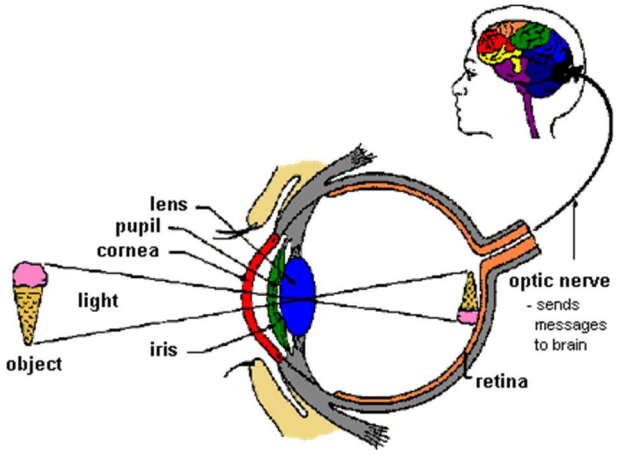

Figure 2.2. Processing of incoming light in the eye.

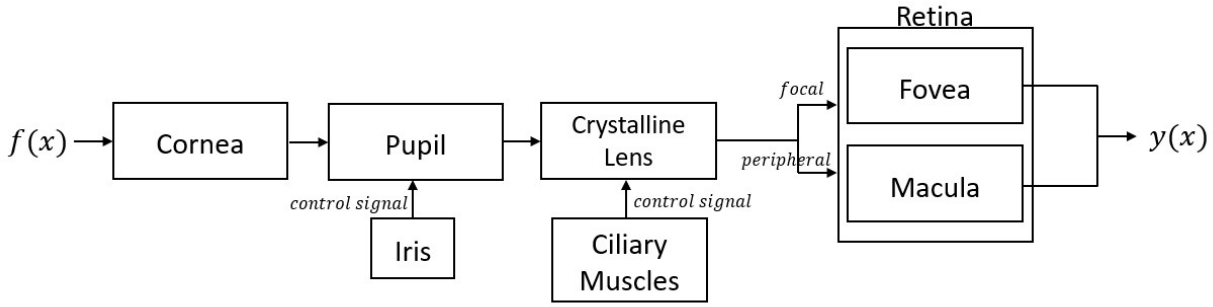

Figure 2.3. Initial image processing in the eye.

2.1.3 Physical Design Space

Figure 2.4 represents the eye with the main geometrical and optical information. Refractive indices are shown in blue, the curvature radii in black, and the appropriate distance in red. It is important to note that every eye is intrinsically unique. However, unlike many other parts of the body, the size of the eye does not vary significantly with gender, age, or ethnic background [25]. The cornea is an approximately spherical section with an anterior radius of curvature of 7.8 mm, posterior radius of curvature of 6.5 mm, and refractive index of 1.3771 [26]. The lens is a biconvex lens with radii of curvature of 10.2 mm and 6.0 mm for the anterior and posterior surfaces [26]. An average eye has approximate dimensions of 3.05 mm, 4 mm, and 16.6 mm for the outer, anterior, and posterior layers, respectively, and has an axial length of 24.2 mm [23].

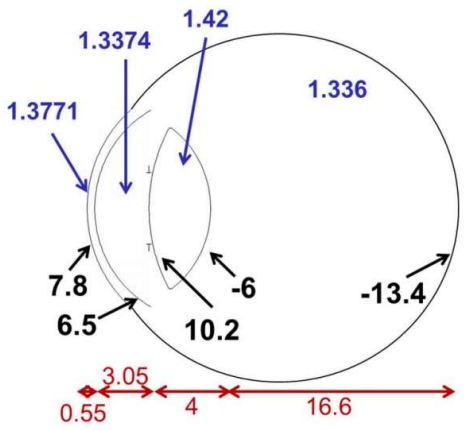

Figure 2.4. Schematic representation of the main geometrical and optical dimensions of the eye.

Figure 2.5 shows the relative size comparison of the proposed implant components. Because the microdisplay will be fixed right in the place of the crystalline lens, the length and the width of the projector must be less than 10 mm. To save room for any additional focusing mechanism, the thickness of the display cannot be more than 1 mm. Because there is no available space inside the eyeball, the projector circuit, as well as the receiver circuit and the antenna, will be placed inside the retroauricular region as shown in Fig. 1.7. This region will allow maximum physical space of 60 mm by 30 mm by 2 mm for our extraocular subcutaneous components [27].

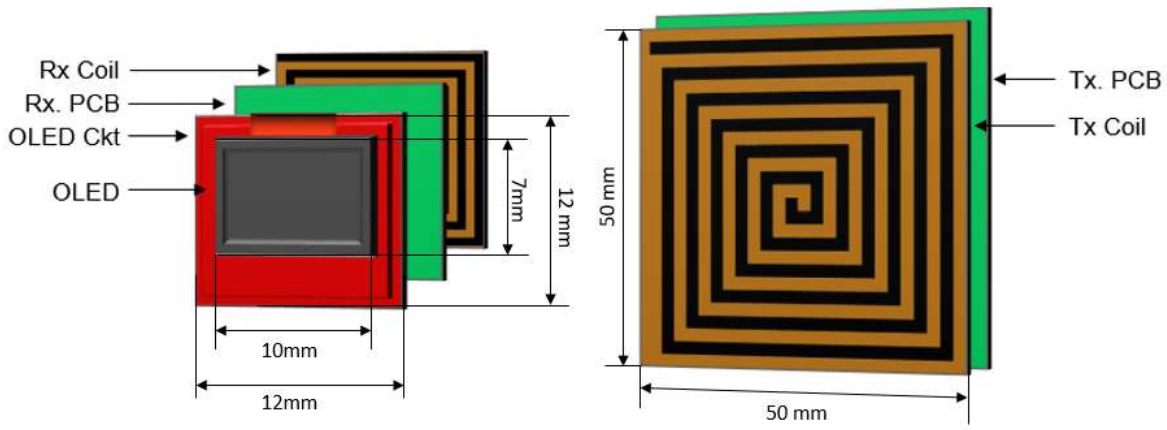

Figure 2.5. Relative size comparison of the major components required for the proposed implant device.

2.2 Radio Frequency Radiation Safety

According to a report by the International Telecommunication Union (ITU), 95% of the global population (seven billion people) live in a mobile-cellular network covered area [28]. As the use

of wireless digital technology proliferated during the last couple of decades, so did the public concern about the influence of the electromagnetic fields (EMFs) on the human body. Many studies have been done to identify the potential effect of various frequencies of EMF on human health, and multiple EMF guidelines have been set forth by various government agencies.

2.2.1 Effect of RF Radiation on Human Health

EMF radiation can be categorized into two different types: lower frequency EMF radiation, and high-frequency EMF radiation. The lower frequency EMF (LF-EMF) is low- to mid-range frequency radiation ranging from the extreme low frequency (ELF) to the microwave frequency (1-300 GHz). Due to the lack of energy per quantum to ionize atoms or molecules, LF-EMF is categorized as non-ionizing radiation.

In contrast, the high-frequency EMF (HF-EMF) is mid- to high-range frequency radiation, ranging from the infrared radiation to the gamma rays (300 GHz-10^{19} Hz). Many studies have revealed that the HF-EMFs have enough energy to penetrate human skin and to potentially lead to irreversible cellular and DNA damage [29]. Though the immediate health effects of HF-EMF apply to its overall frequencies, the potential health effect of LF-EMF radiation is quite frequency dependent. For example, the static fields, ranging from 0~10 MHz have been found to have no biological consequences [30]. However, EMFs operating in some of the RF and microwave frequencies were found to warm up exposed tissues [31]. Though it may be trivial to general parts of the body, increased heating from radiation is very dangerous to the eyes due to their relative lack of available blood flow to dissipate the excessive heat load.

2.2.2 EMF Health Standards

It is well known that significant thermal damage can occur in the sensitive tissue under conditions of partial-body exposure to intense EMF. The eye is the most sensitive organs to microwave heating. Over the decades, extensive research has been carried out on the effect of temperature increase in the eye [33],[34]. Studies have shown that a standing human adult absorbs the most RF energy at EMF of 80-100Mz due to the resonance effect [35]. This is because RF energy is absorbed more efficiently at the body's resonant frequency and will cause maximum heating. In addition to the 80-100 MHz range, due to the additional longitudinal resonances at 1 GHz near the surface of the body, it is crucial to keep the operating frequency below this range.

Furthermore, studies done on microwave EMF from 2.4 to 5 GHz [36]–[40] reported that prolonged exposure to these frequencies has resulted in oxidative stress, elevated apoptotic markers (programmed cell death), cellular DNA damage, and a significant increase in the risk of developing brain cancer. In May 2011, the International Agency for Research on Cancer (IARC) evaluated cancer risks from high RF and microwave frequencies and classified these frequencies EMF as Group 2B human carcinogens [41].

The amount of the RF energy absorbed in the body is called the specific absorption rate (SAR) and is expressed in units of watts per kilogram (W/kg). For harmonically varying EMF, the SAR is defined as:

$$SAR = \frac{\sigma}{2\rho}|\hat{E}|^2 = \frac{\sigma}{2\rho}(|\hat{E}_x|^2 + |\hat{E}_y|^2 + |\hat{E}_z|^2)$$

where $\hat{E}_x, \hat{E}_y, \hat{E}_z$ are the peak values of the electric-field components σ and ρ, denoting the conductivity and mass density of the tissue.

Recently, to review the scientific literature concerning the biological effects of EMF and to bridge the gap between health and RF technology, various organizations and countries have developed exposure standards for RF/microwave EMF. The standards recommend safe levels of exposure, and in the United States, the Federal Communications Commission (FCC) has adopted a guideline from the National Council on Radiation Protection and Measurements (NCRP) and the Institute of Electrical and Electronics Engineers (IEEE). Many countries in Europe use the exposure guideline from the International Commission on Nonionizing Radiation Protection (ICNIRP) which is generally similar to the NCRP and the IEEE guidelines.

In choosing the safe operating frequency, a new EM exposure limit guideline from the IEEE comes in quite handy. As shown in Fig. 2.6, the new IEEE guideline recommends specific frequency, and time-dependent maximum permitted exposure levels [42]. Unlike the old standard published in 1991, this new guideline offers a separate electric field (E) and magnetic field (H) standards.

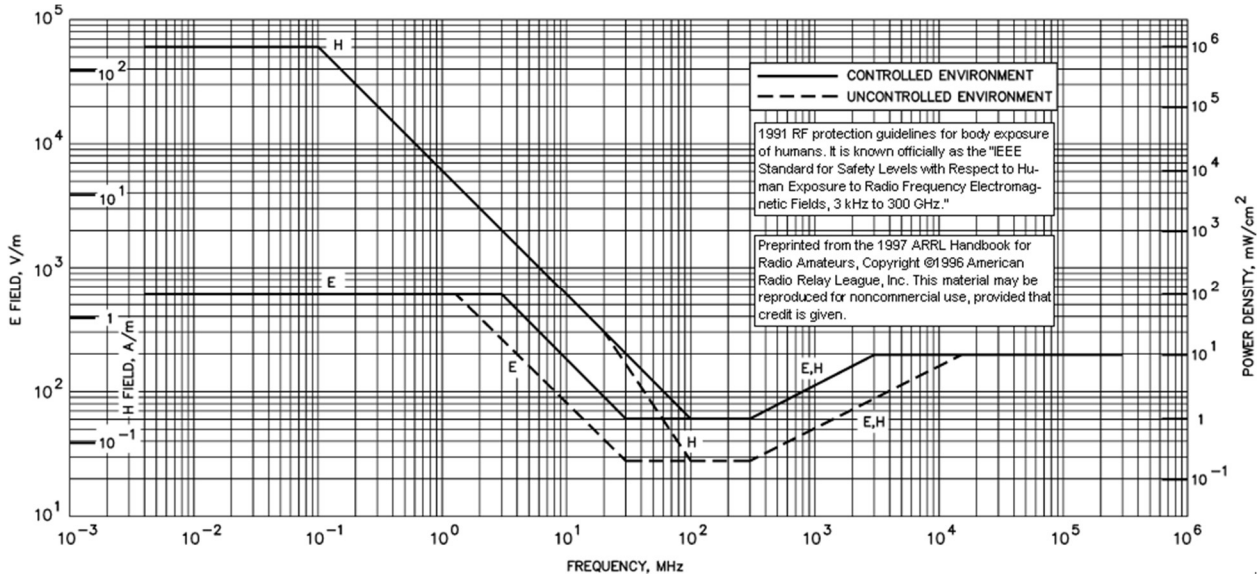

Figure 2.6. New IEEE EMF Exposure standard.

Given that the adult head has a resonant frequency of 400 MHz, the lowest E-field exposure occurs at frequencies 10 to 300 MHz. The lowest H-field exposure occurs at frequencies 20 to 300 MHz. Higher power densities are permitted at frequencies below 30 MHz and above 300 MHz for E-field and below 50 MHz for H-field. This result is based on the assumption that most of the body will not resonate at these frequencies and thus will, in turn, avoid absorbing a lot of energy. After a thorough examination of the EMF effect on patients, we designed the proposed EII device to operate at a carrier frequency of 20 MHz.

Chapter 3: Device Design

Study of the design space revealed that the intraocular region allows the safest maximum length-width-thickness space of 10 mm-10 mm-1 mm inside the eye and the maximum volume of 60 mm-30 mm-2 mm inside the retroauricular region. In addition, the study revealed that the most reliable and safe operating frequency for the wireless link is at 20 MHz, with SAR of 5 W/kg. Given these constraints, the proposed EII device has been designed and will be discussed in detail. To illustrate the proof-of-concept (PoC) of the invention, multiple generations of the physical prototype have been constructed using commercially available components.

3.1 Full Device Design

As shown in Fig. 1.3 and Fig. 1.6c, a diseased cornea completely blocks the incoming light into the eye. The main idea of the proposed device is to bypass the opacified cornea and to project artificial light on to the retina, thereby restoring vision to the patient. This is achieved by using an external camera to capture the incoming light (image) and wirelessly transmitting the image data to an implanted device. The implant device then processes the data and projects the image onto the retina, artificially stimulating the photoreceptors and creating a vision of the image.

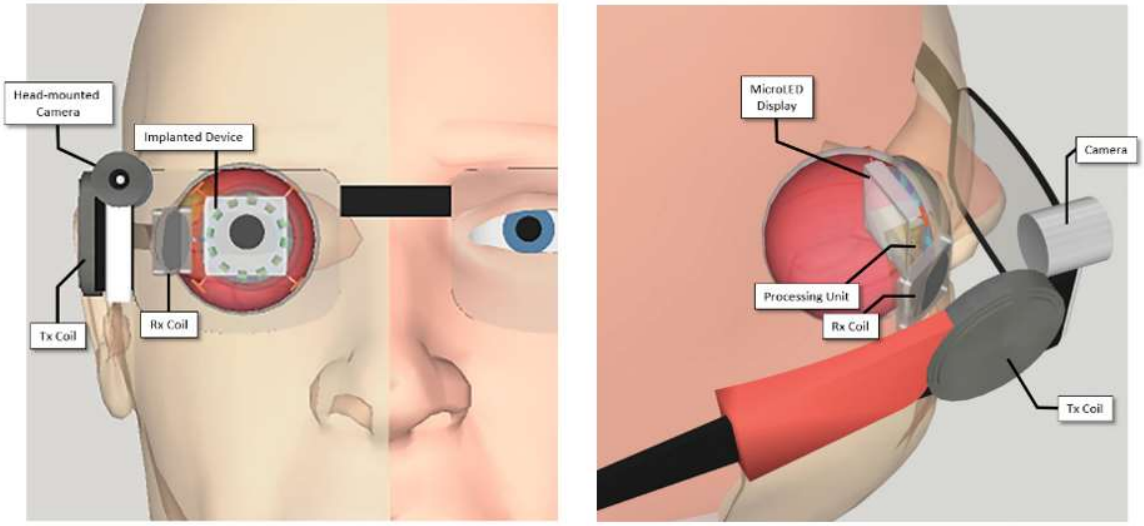

Figure 3.1. 3D drawing of the proposed intraocular device.

Figures 3.1 and 3.2 illustrate the 3D conceptual drawing and the system architecture of the device respectively. First, the glasses-mounted CCD/CMOS camera captures an image. The data is then

coded into a stream of asynchronous serial data and amplitude modulated (ASK) with a 20 MHz carrier signal and transmitted to the in-body receiver via inductive electromagnetic coupling. Next, the receiver simultaneously extracts power from and demodulates the message signal and transfers the input data to the digital signal processing (DSP) unit. The DSP, along with the encoder unit, will process the data and control the output of the micro projector. The micro projector will stimulate the appropriate photoreceptors on the retina using lights to reconstruct the input image.

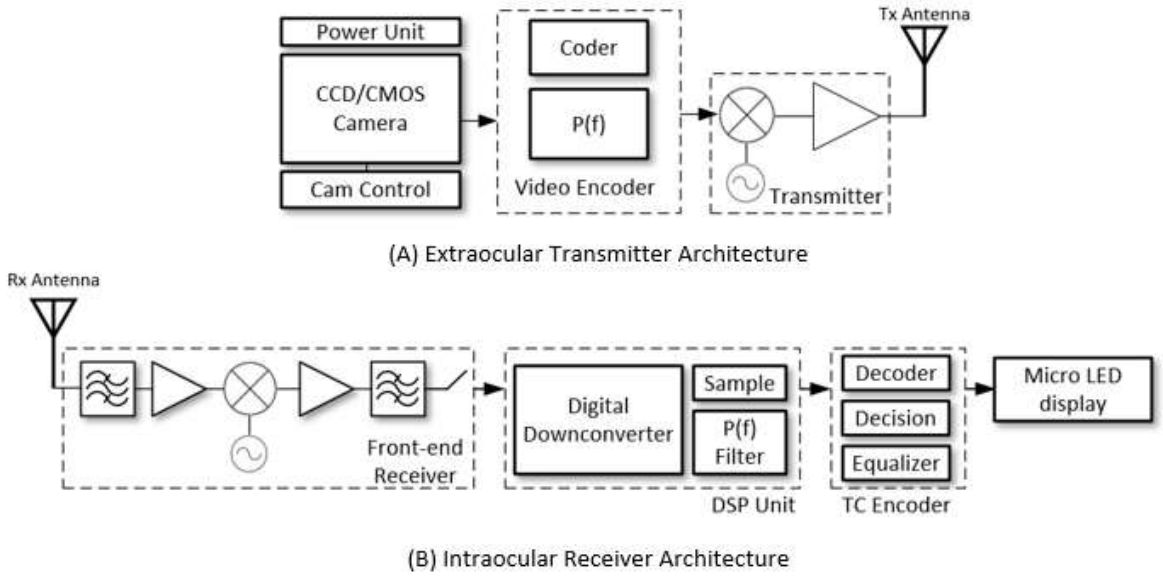

Figure 3.2. The (A) external transmitter and (B) internal receiver architecture of the proposed intraocular device.

To address the form factor and the health-safety restriction, more design emphasis was put into designing the interbody receiver architecture (Fig. 3.2b). The current state-of-the-art micro-OLED displays have form factors of 7x10x1 mm^3 [43]. Since the maximum safe working space is only 10x10x1 mm^3, there is insufficient space within the intraocular region for both the receiver and the OLED display This problem is addressed by only fixing the microdisplay inside the eye, allocating all receiver units to the retroauricular region and connecting the two units via flat flexible cables as shown in Fig. 3.3a. For safe surgical suturing and closing of the tissue of the eye, a specially designed multi-lead wire connector shown in Fig. 3.3b is used to pass the wires through the eye.

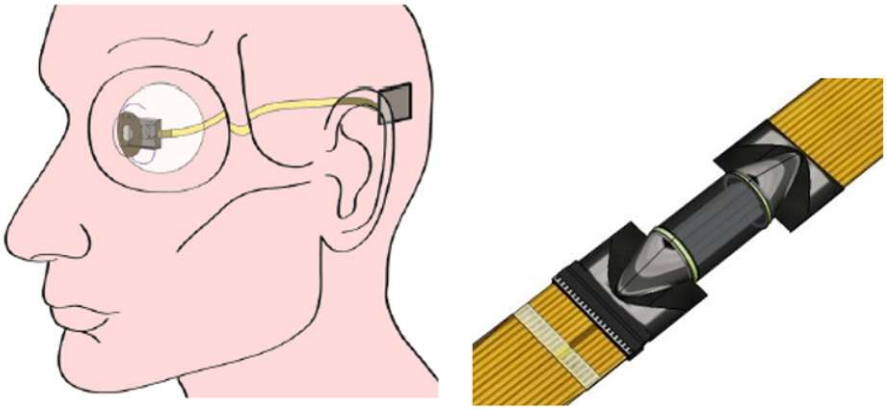

(A) (B)

Figure 3.3 Proposed receiver component allocation: (A) side view of the allocated receiver, (B) special connector designed to pass flat wires through the eye.

The micro-OLED display is shown in Fig 3.4. The display unit has the form factor of 7 mm x 10 mm x 1 mm and has a resolution of 1280 x 720 pixels and can create a light field image of 256 x 144 pixels onto the retina. This image resolution is three orders of magnitude greater than that of the Argus II (6 x 10 pixel field image resolution). A focusing lens replaces the function of the human crystalline lens and focuses the image from the display onto the retina for clear vision.

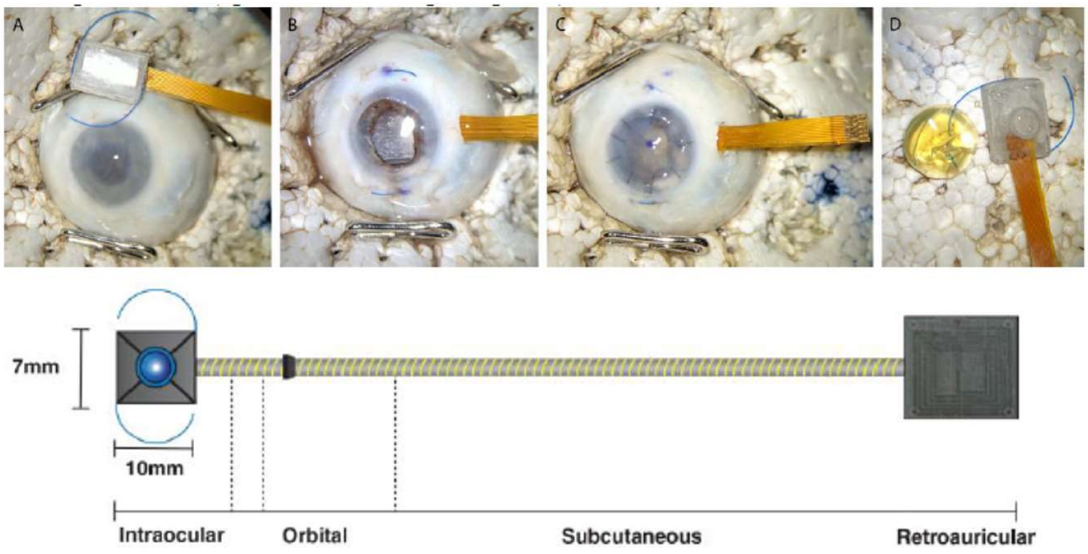

Figure 3.4. Microprojector, waterproof cable, and receiver with surgically implanted view.

3.2 Device Proof of Concept

In order to test the feasibility of the idea and the design or the intra/extraocular architecure, an experimental proof of concept was first demonstrated using commercially available devices and external components without consideration of component size. Figure 3.5 shows the first-phase PoC prototype of the invention. An 8 megapixel, Raspberry Pi Camera V2 with Sony IMX219 image sensor was used to capture 1080p30 static images which were then processed using the Raspberry Pi- Model B- ARMv8 microcontroller. The wireless power link was implemented using WPC 1.2 (Qi) compliant transmitter and receiver kits from Integrated Device Technology (IDT), and the wireless data link was implemented using Pi-internal Bluetooth 4.0. The receiver processor was also implemented with the Raspberry Pi- Model B- ARMv8 microcontroller and the display was constructed using Adafruit Pi TFT 2.2" HAT display with an ST7735R breakout board.

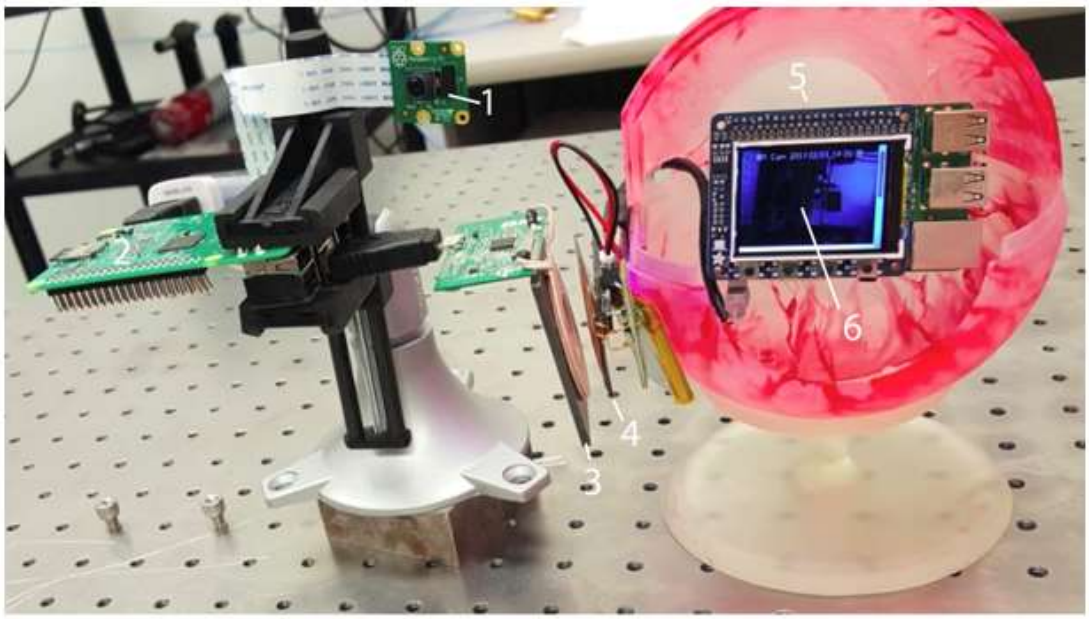

Figure 3.5 First-generation of the PoC prototype of the proposed EII prosthetic. In this fully functional prototype, built with off-the-shelf components, a camera (1) captures video which is processed by transmitter processor (2) and sent via transmitter coil (3) to receiver coil (4). This signal is then processed by receiver processor (5) and displayed in intraocular display (6). The focusing mechanism is not shown.

The first-phase prototype successfully transmitted 320 x 240-pixel video from the camera to the display at 25 frames-per-second (fps) and transmitted 5 W Qi-compliant wireless power at 205 kHz. The success of the first-phase device proved the feasibility of wirelessly transmitting visual data to the eye.

The second-phase prototype aimed to simplify and miniaturize the bulky display and processor components. The 2.2” HAT display used in the first PoC was orders of magnitude larger than the form factor limitation at 65 mm x 57 mm x 6 mm, and thus replaced by the much smaller ECX339A LCD Microdisplay with dimension of 10 mm x 7mm x 4mm. Additionally, the processor units were replaced by Pi-Zero which is half the size of the Pi-B but can still transmit, receive, and process high-resolution video at the desired 25 fps rate. Figure 3.6 shows the second-generation PoC prototype of the device.

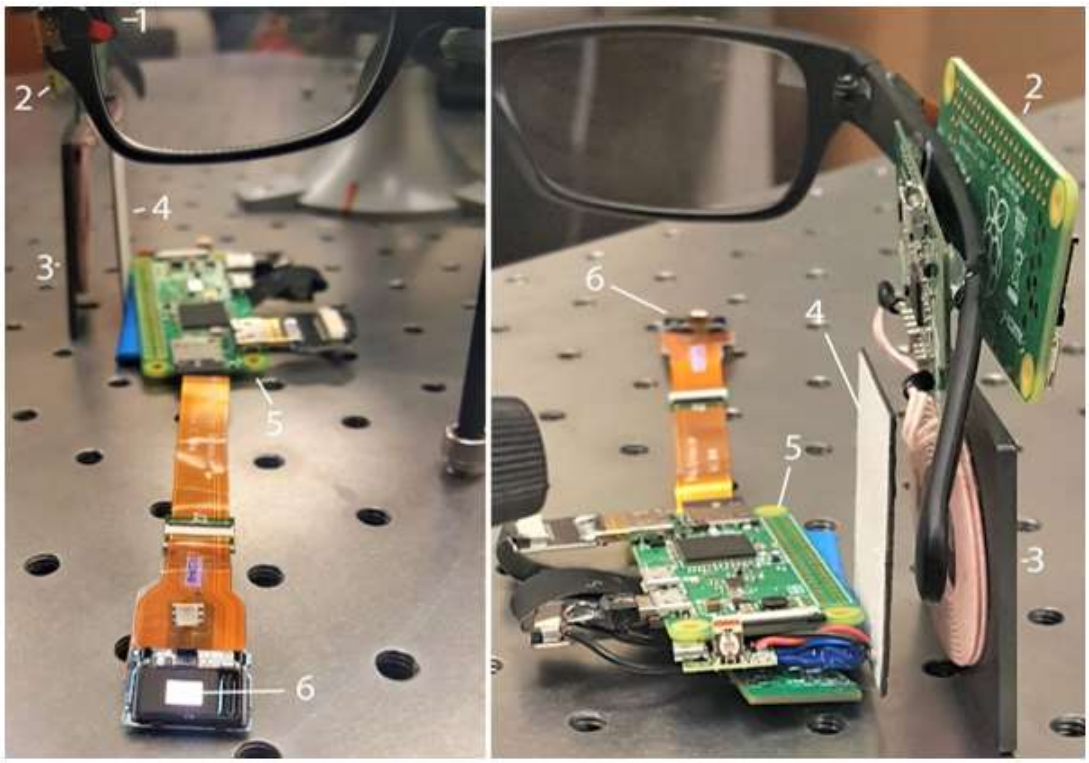

Figure 3.6 Second-generation PoC prototype of the proposed EII prosthetic. In this fully functional prototype, built with off the shelf components, a camera (1) captures video which is processed by transmitter processor (2) and sent via transmitter coil (3) to receiver coil (4). This signal is then processed by receiver processor (5) and displayed in intraocular display (6).

The design of the third-generation PoC prototype focuses on the redesign of the intraocular micro-LED with additional components such as the focusing lens, polarizing filter, and a light diffuser to project and focus the displayed images onto the retina as seen in Fig. 3.7. An experimental result (Fig. 3.8) shows that an image is successfully projected onto a spherical, retina-like screen at distance of 16 mm (approximate distance from the crystalline lens to the retina). The focusing array

can be easily modified by varying the power of the lens. The third-generation PoC prototype successfully projected a 256 x 144-pixel image onto the retina-like screen at 25 fps at a distance of 6 mm.

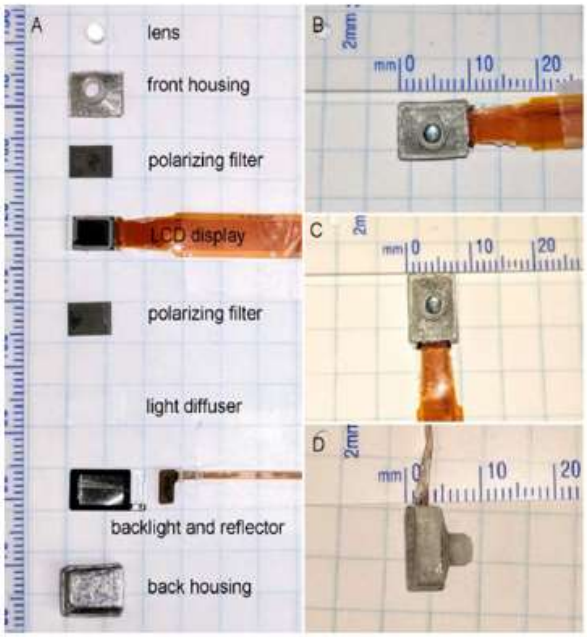

Figure 3.7 (A) Components of the micro projector from various perspectives, scale in mm, in (B), (C), (D).

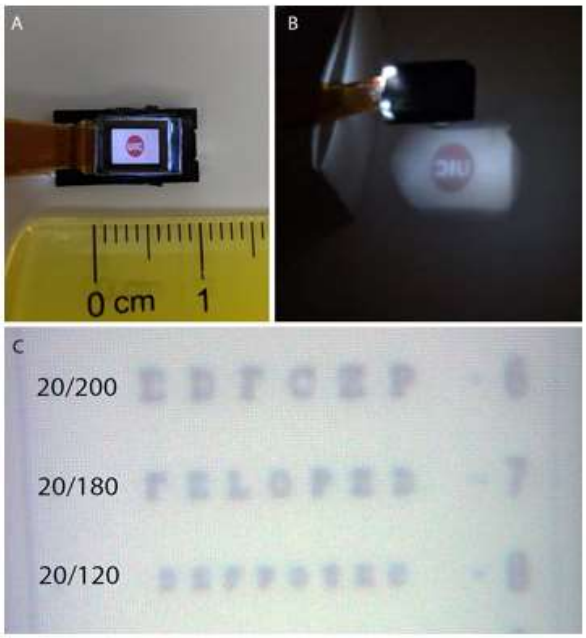

Figure 3.8 (A) Microdisplay without the focusing components, (B) projection using the additional focusing components, (C) visual acuity demonstration.

After successfully projecting the miniaturized display with the third-phase prototype, the fourth-generation of the device focuses on the simplification of the wireless link. The commercial Tx and Rx system from IDT provided efficient power transfer to the microcontrollers but is too large for the available 60 mm x 30 mm x 2 mm device space in the retroauricular region. Additionally, its 250 kHz operating frequency is well below the optimal safe operating frequency of 20 MHz. Furthermore, the current commercially available units are only capable of wireless power transmission and do not support the necessary wireless data transmission. Therefore, a custom system for simultaneous wireless power and data transmission is designed and implemented to meet the design specifications as discussed in the next chapter.

Chapter 4: Dual Coil System

The first three generations of the prototype sought to find appropriate commercially available components from various sources and connect them into one system. However, while sufficiently small commercial displays are available, commercial devices capable of simultaneous wireless power and data transmission while also meeting the size, frequency and power constraints for micro-implant devices are currently nonexistent. Therefore, a wireless power and data exchange system is custom designed and built from the ground up as demonstrated in this chapter.

4.1 Characterization and Identification of Inductive EM Coupling Scheme

4.1.1 Identifying Ideal Coupling Scheme

Since power transfer decreases cubically with distance, a short distance near-field setup is implemented to maximize power efficiency. For near-field signal transfer, the coupling between devices can be conducted using either an electric and/or magnetic scheme. Electric coupling, or capacitive coupling, is the signal transfer between different apparatuses using a capacitor. The coupling can be effectively characterized by the short-circuit admittance Y-parameters. Given an apparatus with port voltage and current given in Eqns. 4.1 and 4.2, the corresponding electric coupling can be characterized by the two-port Y-parameter (Eqns. 4.3-4.6).

$$I_1 = Y_{11}V_1 + Y_{12}V_2 \tag{4.1}$$

$$I_2 = Y_{21}V_1 + Y_{22}V_2 \tag{4.2}$$

where

$$Y_{11} = \frac{I_1}{V_1}\Big|_{V_2=0}\text{; Input admittance, output shorted} \tag{4.3}$$

$$Y_{12} = \frac{I_1}{V_2}\Big|_{V_1=0}\text{; Reverse transfer admittance, input shorted} \tag{4.4}$$

$$Y_{21} = \frac{I_2}{V_1}\Big|_{V_2=0}\text{; Forward transfer admittance, output shorted} \tag{4.5}$$

$$Y_{22} = \frac{I_2}{V_2}\Big|_{V_1=0}\text{; Output admittance, input shorted} \tag{4.6}$$

Or, for the general case of the N-port network,

$$Y_{nm} = \frac{I_n}{V_m}\Big|_{V_k=0} \tag{4.7}$$

Given that the two ports are reciprocal, the network can be expressed in an equivalent pi circuit model using the corresponding Y-parameters as shown in Fig. 4.1a.

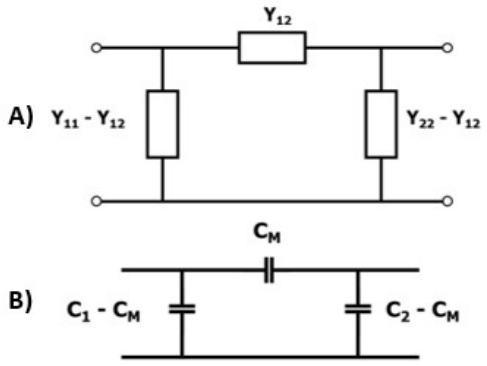

Figure 4.1. Pi model of the electrically coupled system regarding the (A) Y-parameters or (B) equivalent capacitance values.

We can use this to model our electrically coupled system as shown in Fig. 4.1b. C_1 and C_2 represent the self-capacitances of the reactive elements on the transmitter and the receiver, and C_M represents the mutual capacitance formed between the elements. For the electric coupled system, a coupling coefficient figure of merit is defined as

$$k_e = \frac{C_M}{\sqrt{C_1 C_2}} \tag{4.8}$$

which relates the coupled and stored electric energy of the resonant system. Values of k vary from 0 (isolation), when no energy is shared between capacitors, to k = 1 (perfect coupling). In our application, a high coupling coefficient is desirable because we want as much signal to be transferred from the transmitter to the receiver as possible.

In contrast to the electric/capacitive coupling, magnetically coupling results from electromagnetic induction. As a result, the magnetically coupled resonators are effectively characterized by the

open-circuit impedance parameter, the Z-parameter. Given two apparatuses with the port voltage and current given in Eqns. 4.9 and 4.10, the corresponding inductive coupling can be characterized by the two-port Z-parameters defined in Eqns. 4.11-4.14.

$$V_1 = Z_{11}I_1 + Z_{12}I_2 \tag{4.9}$$

$$V_2 = Z_{21}I_1 + Z_{22}I_2 \tag{4.10}$$

where

$$Z_{11} = \frac{V_1}{I_1}\Big|_{I_2=0} \text{; Input impedance, output opened} \tag{4.11}$$

$$Z_{12} = \frac{V_1}{I_2}\Big|_{I_1=0} \text{; Reverse transfer impedance, input opened} \tag{4.12}$$

$$Z_{21} = \frac{V_2}{I_1}\Big|_{I_2=0} \text{; Forward transfer impedance, output opened} \tag{4.13}$$

$$Z_{22} = \frac{V_2}{I_2}\Big|_{I_1=0} \text{; Output impedance, input opened} \tag{4.14}$$

Given that the two ports are reciprocal, the network can be expressed in an equivalent "T" circuit model using the corresponding Z-parameters as shown in Fig 4.2.

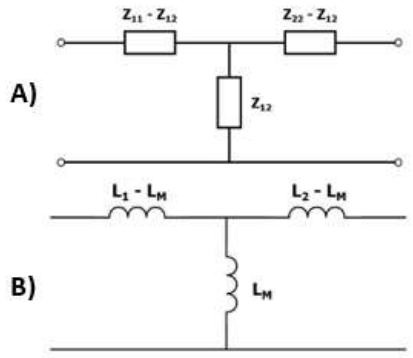

Figure 4.2. T model of the magnetically coupled system regarding the (A) Z-parameters or (B) equivalent inductance values.

From the figure, L_1 and L_2 represent the self-inductance of the reactive elements of the Tx and Rx, and L_M represents the mutual inductance between the elements. The resulting coupling coefficient is defined as:

$$k_m = \frac{L_M}{\sqrt{L_1 L_2}} \tag{4.15}$$

Given a choice between inductively and capacitively coupling resonators, the design choice will largely depend on the specific application. Even though both systems can be used interchangeably by easily converting Y-parameters to Z-parameters, or from pi model to the T model, at high frequencies, inductors typically have higher loss than the capacitors and are therefore less efficient. However, one of the most crucial design parameters for our device is the extreme space limitation. The amount of transfer power efficiency in capacitive coupling heavily depends on the capacitance between the plates, the physical size of the plates, and the operating frequency [7]; this makes the coupling scheme less suitable for lower frequency, small form factor application. Given that inductors are more flexible concerning the range of inductance values for a given area, we design our wireless link as a magnetically coupled system.

4.1.2 Power Transfer Efficiency

In addition to space considerations, the wireless power transfer efficiency (PTE) must also be considered, since low PTE will significantly attenuate the received signal and make the data impossible to recover. PTE gives information on the power delivered to the load compared to the power transmitted by the source, and maximum PTE is a critical design consideration for any WPT application. Figure 4.3 illustrates the high dependence of PTE on the axial distance, which is defined as the distance between the source and the load [44].

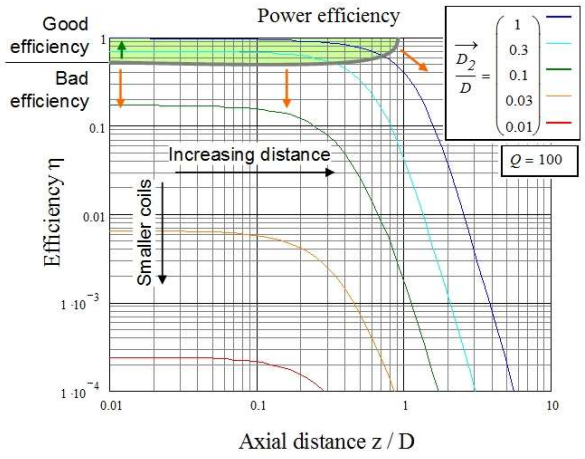

Figure 4.3 Power efficiency for an inductive power transfer system consisting of loop inductors concerning their axial distance *z* calculated for a standard inductor quality factor of *Q*=100.

The PTE of a link can be directly computed efficiently using the two-port scattering parameters, or S-parameters. For the two-port system shown in Fig. 4.4, we can determine our S-parameters as

$$b_1 = S_{11}a_1 + S_{12}a_2 \tag{4.16}$$

$$b_2 = S_{21}a_1 + S_{22}a_2 \tag{4.17}$$

where

$$S_{11} = \frac{b_1}{a_1}\Big|_{a_2=0} \tag{4.18}$$

$$S_{12} = \frac{b_1}{a_2}\Big|_{a_1=0} \tag{4.19}$$

$$S_{21} = \frac{b_2}{a_1}\Big|_{a_2=0} \tag{4.20}$$

$$S_{22} = \frac{b_2}{a_2}\Big|_{a_1=0} \tag{4.21}$$

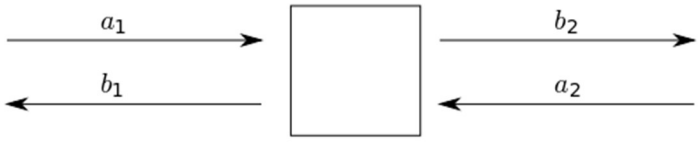

Figure 4.4 2-Port system with input wave (a_i) and output wave (b_i)

The wave variables a_i, and b_i are normalized parameters with units of [watts]$^{1/2}$. Incident waves that are going into the network are designated by a_i, whereas reflected or scattered waves leaving the network are designated by b_i, where 'i' is an index that references a specific port. The advantage of using the S-parameter for our application is that the parameters can be easily and reliably measured at high frequencies. A comprehensive overview of S-parameters can be found in [45].

Due to the strict size constraint, a simple two-coil system is implemented for the wireless link. In a two-coil inductive resonance system as shown in Fig 4.5, the Tx inductor is inductively coupled to an Rx inductor via magnetically enhanced resonance. The resonance is facilitated by loading the two inductors with its corresponding resonant capacitances. This process will form two LC

resonators in the system that are coupled through the mutual inductance (M_{12}) and in combination will resemble a coupled resonator-based filter.

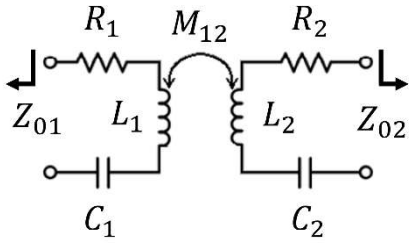

Figure 4.5 Dual-coil inductive resonance system.

4.2 Coil Antenna Parameter Design

Building on previous work on inductive power transmission links [46]–[51], the basic circuit model from Fig. 4.5 is expanded for our transcutaneous inductive link as illustrated in Fig. 4.6. L_1 is the transmitter coil that is attached to the extraocular component of the system driven by a source depicted by V_s, whereas L_2 is the receiver coil of the implant. The parasitic resistance and capacitance associated with each coil are depicted in Fig 4.6 by lumped elements, R_s and C_P. The capacitors, C_S, are added to form a pair of resonant LC tank circuit with corresponding L at the operating frequency f_o.

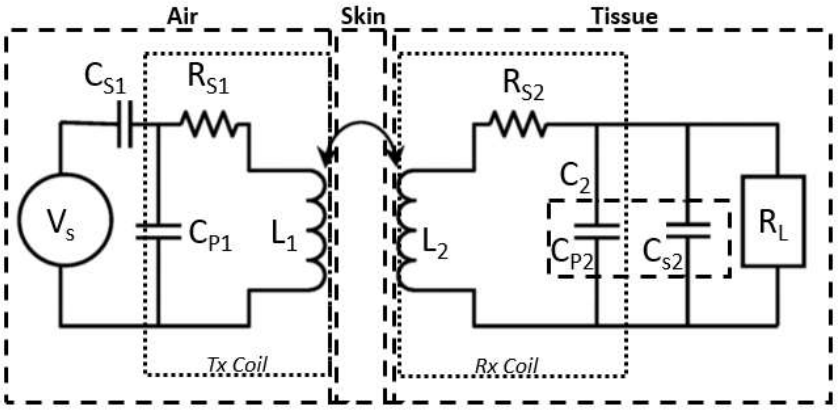

Figure 4.6 Circuit model of the transcutaneous inductive link design.

Historically, coil antennas have been fabricated by winding think wires using winding machinery [51]. However, the extreme footprint limitations in high-performance-implantable devices call for smaller scale coils with high geometrical precision. Thus, instead of winding, many coils are now

fabricated as printed spiral coils (PSCs). PSCs offer flexibilities in coil parameters, rigidity, and size. In this section, we will calculate the physical parameters of our PSCs to formal optimal performance at f_o = 20 MHz.

4.2.1 Quality Factor Calculation

The lumped parasitic components of the printed coils model in Fig 4.6 depends on the geometry, material composition, and surrounding environment of the coil. In this research, square-shaped coils were used mainly for the ease of fabrication. Several closed-form equations have been adopted from [52] for evaluating square-shaped coils using geometrical parameters shown in Fig. 4.7.

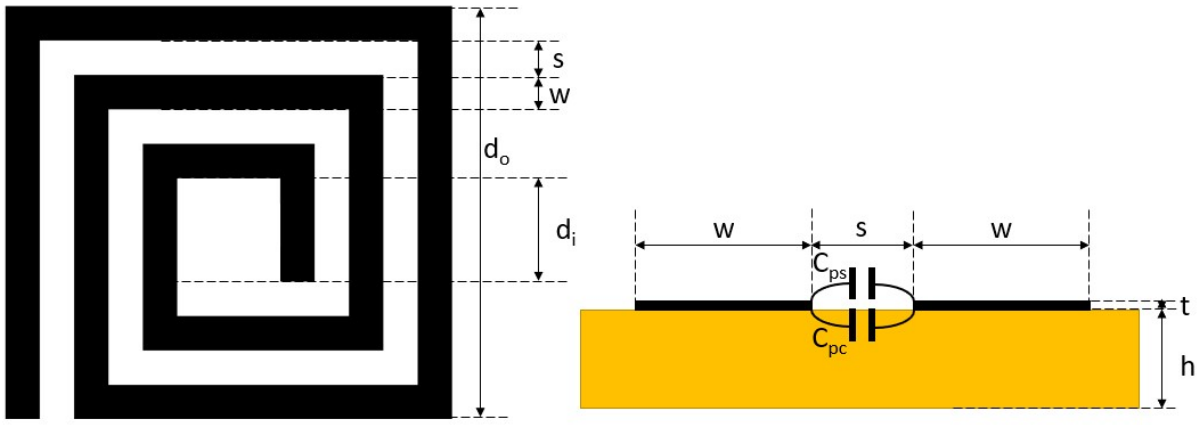

Figure 4.7 Geometrical parameters of a square-shaped printed spiral coil.

Self-inductance L is the ratio of the magnetic flux generated by the conductor and the current passing through it. Using the geometrical parameters of a square-shaped PSC below, we can approximate the self-inductance L

$$L = \frac{1.27\mu_O N^2 d_{avg}}{2}\left[\ln\left(\frac{2.07}{\varphi}\right) + 0.18\varphi + 0.13\varphi^2\right] \tag{4.22}$$

$$\varphi = \frac{d_o - d_i}{d_o + d_i} \tag{4.23}$$

$$d_{avg} = \frac{d_o + d_i}{2} \tag{4.24}$$

where N is the number of turns, d_o and d_i are the outer and inner diameters respectively, and φ is the fill factor. The parasitic resistance of the PSC, R_s, can be calculated by using the DC resistance and the skin depth (δ)

$$R_{dc} = \rho_c \frac{l_c}{wt} \tag{4.25}$$

$$R_s = R_{dc} \frac{t}{\delta(1 - e^{-t/\delta})}, \quad \delta = \sqrt{\frac{\rho_c}{\pi \mu f}} \tag{4.26}$$

where δ is the skin depth and l_c is the length of the conductive trace which can be found by using simple geometry

$$l_c = 4Nd_o - 4Nw - (2N + 1)^2(s + w) \tag{4.27}$$

where t, s, and w are the conductor thickness, line spacing and width respectively, ρ_c is the resistivity of the conductive material and μ is the permeability.

By using the parameters from above, we can calculate the quality factor Q of each coil. It will later be shown in Eqn. 4.37 that high Q coils result in links with high PTE.

$$Q_1 = \frac{\omega L_1}{R_{s1}} \tag{4.28}$$

$$Q_2 = \frac{\omega L_2}{R_{s2}} \tag{4.29}$$

4.2.2 Mutual Inductance Calculation

As seen by the k FoM, a high mutual inductance is essential for efficient wireless coupling. The mutual inductance (M) can be approximated by first finding M between a pair of single-turn coils in parallel planes and then summing up the partial mutual inductance values from additional turns. Partial mutual inductance between a pair of parallel single-turn coils at radii r_i and r_j can be approximated by adopting the method from [53] which uses the complete elliptic integrals of the first and second kind:

$$M_{ij} = \frac{2\mu}{\alpha}\sqrt{r_i r_j}\left[\left(1 - \frac{\alpha^2}{2}\right)K(\alpha) - E(\alpha)\right]\ ;\ \alpha = 2\sqrt{\frac{r_i r_j}{(r_i + r_j)^2 + D^2}} \tag{4.30}$$

where D is the relative distance between the two coils, $K(\alpha), E(\alpha)$ are the complete elliptic integrals of the first and second kind.

After finding the partial mutual inductances between every turn in the coil, the total mutual inductance can be found by summing them:

$$\mathrm{M} = \mathrm{g}\sum_{i=1}^{N1}\sum_{j=1}^{N2} M_{ij}(r_i, r_j, D) \tag{4.31}$$

where g refers to the shape factor. We used g=1.1 from the empirical result in [54].

Using results from Eqn. 4.22 - 4.31, the mutual inductance can also be represented as the coupling coefficient:

$$k = \frac{M}{\sqrt{L_1 L_2}} \tag{4.32}$$

4.2.3 Inductive Link Efficiency Calculation

For an inductive resonator pair, the maximum power transfer efficiency across the link is achieved when both LC-tanks are tuned at the operating frequency

$$\omega = \omega_O = {}^{1}\Big/\sqrt{L_1 C_1} = {}^{1}\Big/\sqrt{L_2 C_2} \tag{4.33}$$

In practice, the secondary coil is loaded with RL, and the quality factor at resonance is found from

$$Q_L = \frac{1}{\frac{R_{s2}}{\omega L_2} + \frac{\omega L_2}{R_L}} = \frac{1}{R_{s2}\sqrt{\frac{C_2}{L_2}} + \frac{1}{R_L}\sqrt{\frac{L_2}{C_2}}} \tag{4.34}$$

Considering the above equation, Ko et al. [46] demonstrated that antenna efficiency (η) can be defined as

$$\eta_1 = \frac{P_1}{P_S} = \frac{k^2 Q_1 Q_L}{1 + k^2 Q_1 Q_L} \tag{4.35}$$

$$\eta_2 = \frac{P_L}{P_2} = \frac{Q_L}{Q_2 + Q_L} \tag{4.36}$$

where P_1 and P_2 are the transmitted and received power respectively and P_S and P_L are the powers delivered to the source and load respectively. Therefore, from Eqns. 4.35 and 4.36, the total link PTE can be expressed as [55]:

$$PTE = \eta_{12} = \eta_1 \eta_2 = \frac{k^2 Q_1 Q_L}{1 + k^2 Q_1 Q_L} \frac{Q_L}{Q_2 + Q_L} \tag{4.37}$$

It is important to note that all the parameters above are interrelated. Therefore, parameters in Eqns. 4.22-4.34 are swept using MATLAB for a desired PSC coil pair geometry. Afterward, the 3D model of the two-coil design is constructed in Ansys HFSS.

4.3 Simulation and Implementation

An Rx and Tx coil pair has been designed and optimized for a muscle tissue environment. The material properties of the channel media are shown in Table 4.1 and have been derived following work in [56], [57]. An iterative design procedure described in [54] has been adopted, which starts from the design constraints and initial conditions discussed in previous chapters and ends with optimal geometries of coil parameters that maximize η_{12}. However, because this method restricts the resulting coil-pair to be the same size, it was only adopted to give approximate PTE for our application. A 40 mm x 50 mm x 1.5 mm Tx coil and a 10.25 mm x 10.25 mm x 1.5mm Rx coil have been designed at nominal coupling distance of d=5mm. The operating carrier frequency is set at 20 MHz to comply with the design safety specification. As shown in Fig. 4.8, the resulting parameters are simulated using Ansys HFSS to verify and fine-tune the theoretical calculation.

Table 4.1 Material properties derived from [56], [57].

MATERIAL PROPERTIES

Material	Air	Saline	Muscle	FR4	Silicone
f [MHz]	13.56	13.56	13.56	13.56	13.56
σ [S/m]	0	0.60	0.58	1.33e-4	2.26e-6
ε_r	1	78	136	4.4	3.0
$tan(\delta)$	0	10.2	6.0	0.04	0.001

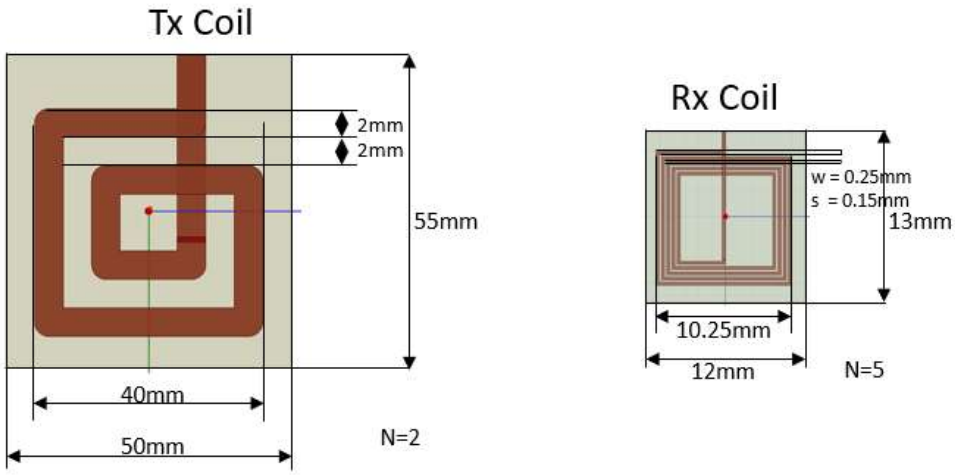

Figure 4.8 Designed coil parameters using Matlab simulation.

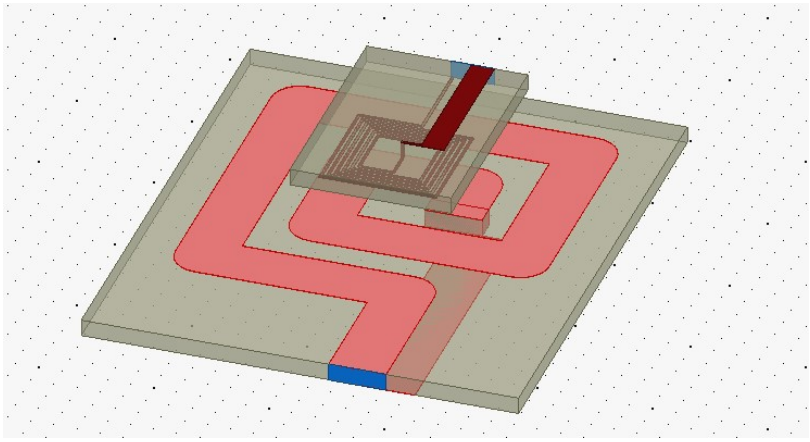

Figure 4.9 HFSS model of a two-coil system.

A 3-dimensional model of the two-coil design is constructed using the Ansys HFSS simulation software and is shown in Fig. 4.9. The design consists of a 40 mm by 40 mm transmitting coil and a 10.25 mm by 10.25 mm receiving coil. The separation distance of the coils was kept at 5 mm. The coil parameters used in HFSS were used to print the coils onto an FR4 board. Figure 4.10 shows the printed PSC and the measurement setup.

The experiment used a network analyzer to measure the S-parameters of the coupled PSC pair, while they were separated at the desired coupling distance using Plexiglass support. The S-parameters from the network analyzer were extracted and converted to find η_{12} using $|S_{12}|^2$. As shown in Fig. 4.11, the experimental value of the coils closely resembled the HFSS simulated result, especially near the operating frequency. However, both experimental and simulated values resulted in low transmission efficiency of -27.5 dB.

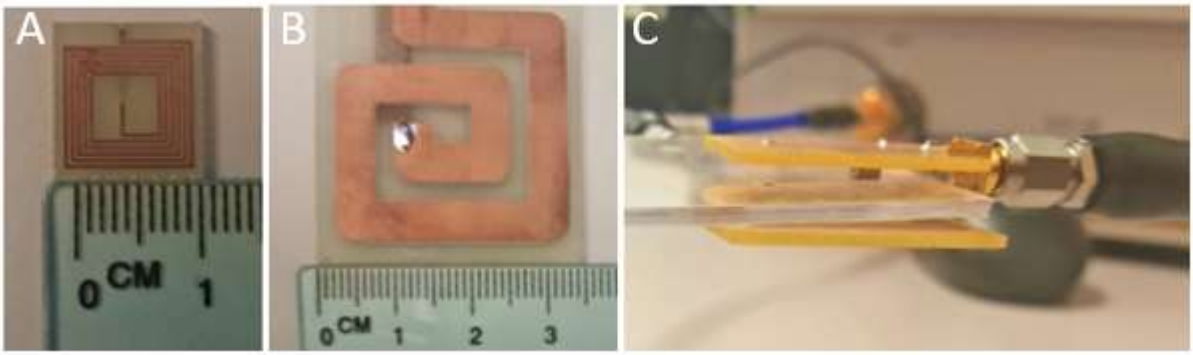

Figure 4.10 Printed receiver and transmitter coils and the experimental setup: (A) receiver coil, (B) transmitter coil, (C) experimental setup of the transmitter and the receiver coil.

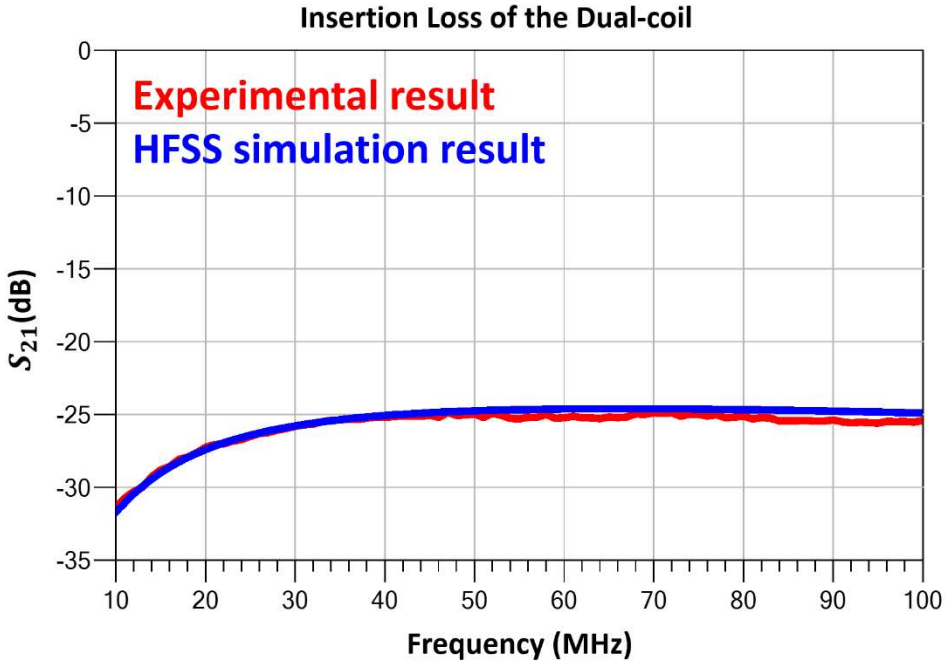

Figure 4.11 HFSS simulations result vs. the experimental result of the dual-coil link.

4.4 Simultaneous Matching Design

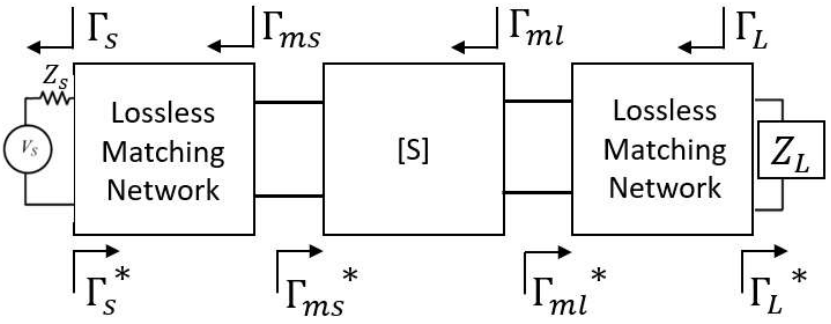

Figure 4.12 Simultaneous conjugate matching scheme.

The low transfer efficiency is improved by using simultaneous conjugate matching on both sides of the antenna (Fig. 4.12). For passive system, the simultaneous conjugate matching networks are designed using calculations below:

$$\Gamma_{in} = \Gamma^*{}_{ms} = S_{11} + \frac{S_{12}S_{21}\Gamma_{ml}}{1 - S_{22}\Gamma_{ml}} \tag{4.38}$$

$$\Gamma_{out} = \Gamma^*{}_{ml} = S_{22} + \frac{S_{12}S_{21}\Gamma_{ms}}{1 - S_{11}\Gamma_{ms}} \tag{4.39}$$

The solution to Eqns. 4.38 and 4.39 is found by using

$$\Gamma_{ms} = \frac{B_1 \pm \sqrt{B_1{}^2 - 4|C_1|^2}}{2C_1};\ \Gamma_{ml} = \frac{B_2 \pm \sqrt{B_2{}^2 - 4|C_2|^2}}{2C_2} \tag{4.40}$$

$$B_1 = 1 + |S_{11}|^2 - |D|^2 - |S_{22}|^2;\ B_2 = 1 + |S_{22}|^2 - |D|^2 - |S_{11}|^2 \tag{4.41}$$

$$C_1 = S_{11} - DS^*{}_{22};\ C_2 = S_{22} - DS^*{}_{11} \tag{4.42}$$

The choice of signs in Eqn. 4.40 is determined by the criteria

$$\Gamma_{ms} < 1 \ \ and \ \ |\Gamma_{ml}| < 1 \tag{4.43}$$

Using the relationship between impedance and reflection the matched impedance values can be found

$$Z = \frac{1+\Gamma}{1-\Gamma} \tag{4.44}$$

$$\Gamma = \frac{Z-1}{Z+1} \tag{4.45}$$

LC matching networks were implemented and simulated using Keysight Advanced Design System (ADS) as shown in Fig. 4.13.

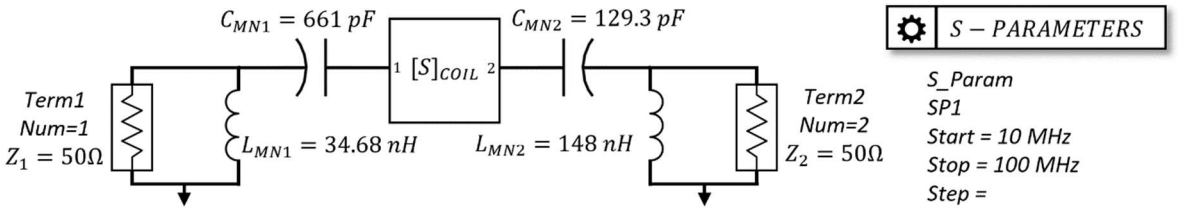

Figure 4.13 ADS simulation of the conjugate simultaneous matching network.

The calculated parameters were modified to support commercially available inductor and capacitor values. The simulated S-parameters were compared to the S-parameters extracted from the network analyzer from the experiment (Fig. 4.14). The result showed an increase of 26 dB in the insertion loss (IL) for the simulated result and an increase of 17 dB for the experimental result compared to the unmatched dual-coil system presented in Section 4.3. In addition, the matched system yielded a decrease of 18 dB and 16 dB for the return loss of the simulated and the experimented values respectively compared to the unmatched case. By calculating the power transfer efficiency using the S_{21} parameter, Fig. 4.15 shows a PTE of 88% and 71% for simulated and experimented coils respectively. In addition, Fig. 4.16 compares the transient output of the perfectly matched (from ADS simulation result), the unmatched (from the experimental result), and the matched (from experimental result) coils respectively.

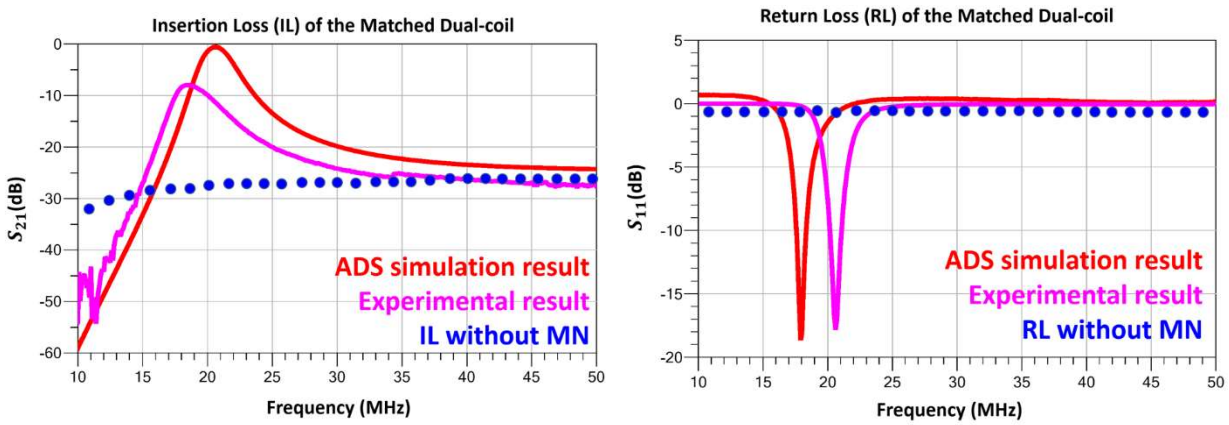

Figure 4.14 Comparison of the S-parameter results from the ADS simulation and the experiment between the matched and unmatched systems.

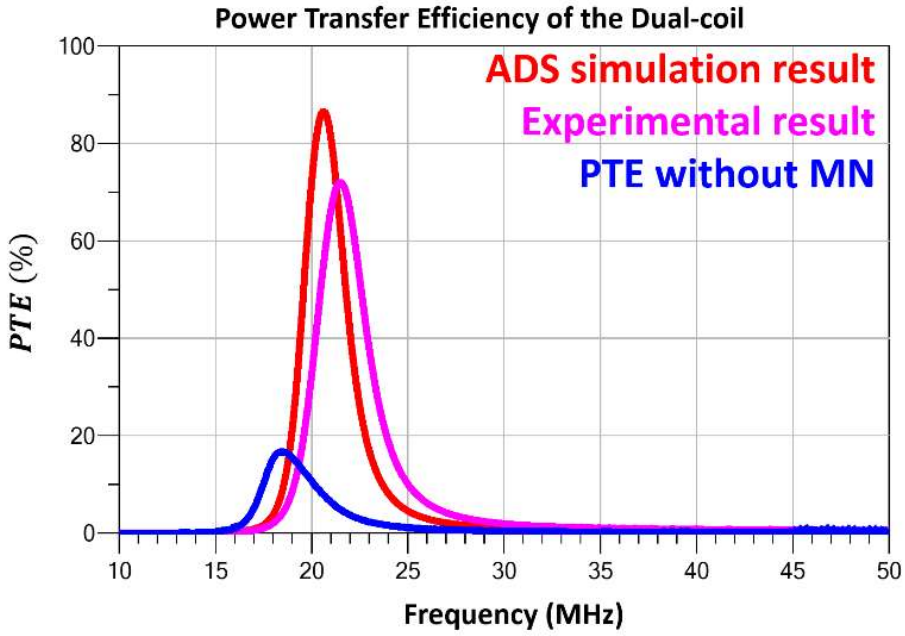

Figure 4.15 Comparison of the PTE data from the ADS simulation and experiment between the matched and unmatched systems.

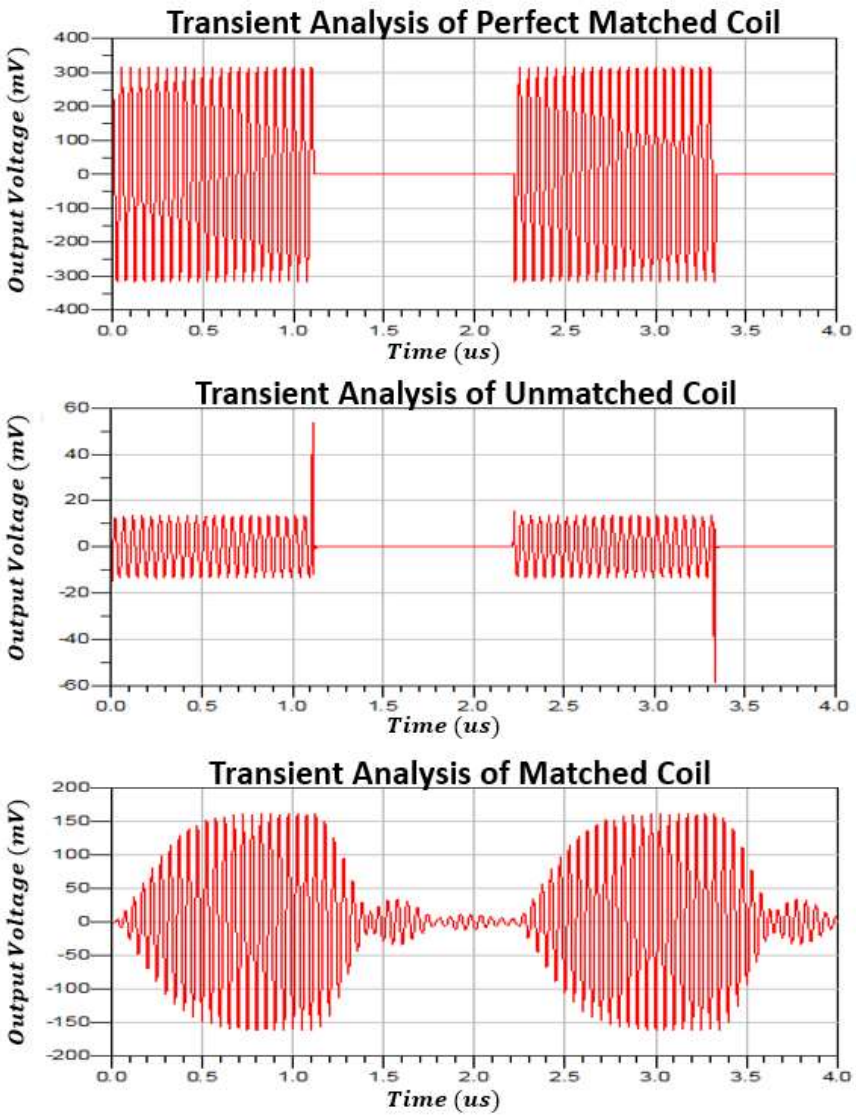

Figure 4.16 Comparison of the transient analysis results from the ADS simulation and the experiment between the matched and unmatched systems.

However, as seen in Fig. 4.17, the PTE is heavily dependent on the distance between the coils. Since the transmitter coil will be fixed on the glasses apparatus, this could cause variation in the distance between the coils. The insertion loss of the coil at different separation distances D is shown in Fig. 4.18. Notice that as the distance increases, the IL drops faster. This problem can be mitigated by effectively designing the glasses apparatus to firmly fit onto the patient's head such that distance variation is minimized.

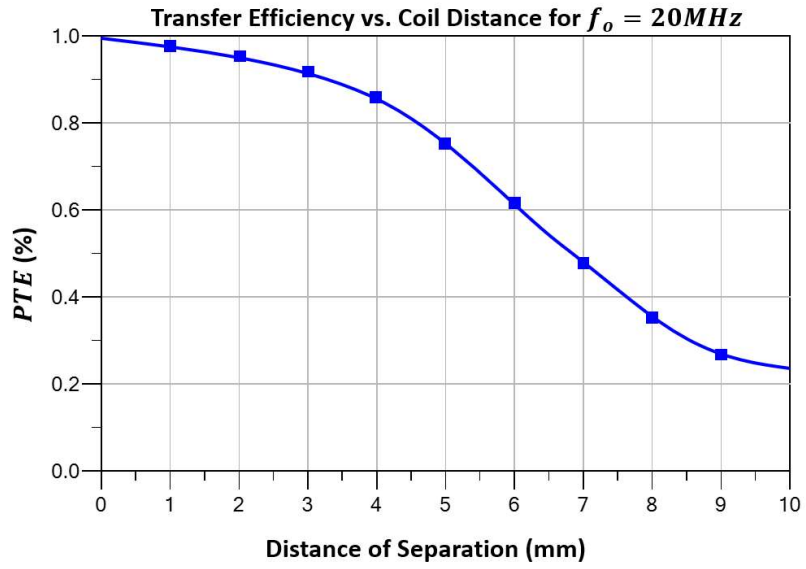

Figure 4.17. PTE vs. coil separation distance for an operating frequency of 20 MHz.

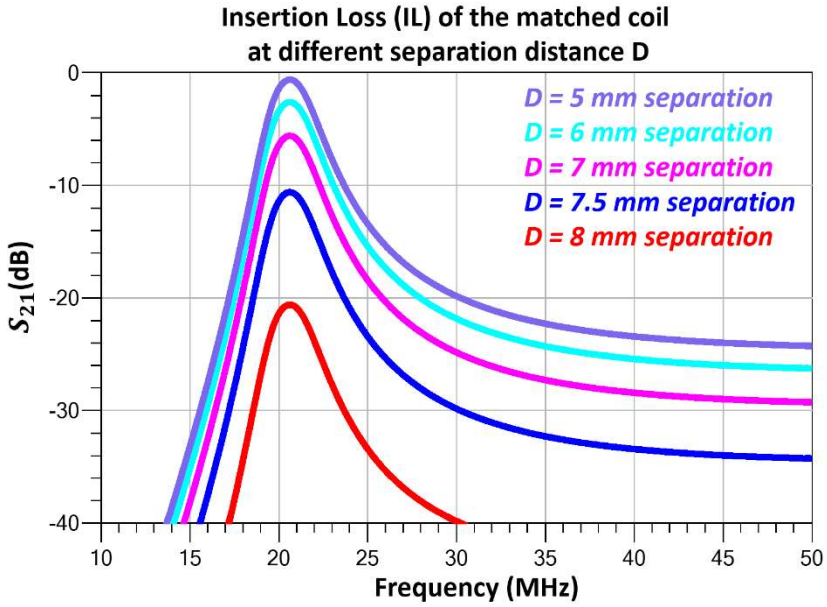

Figure 4.18. Insertion loss study of the matched coil under different separation distances.

Chapter 5: Receiver Design

Unlike the transmitter system, which has more design freedom due to its location outside of the body, the receiver unit must receive, demodulate and process image data while still fitting comfortably with the retroauricular region of the skull. To minimize device size, only one antenna is used for reception. Thus, a robust front-end receiver that can simultaneously harvest power and demodulate the received signal is needed. The receiver requires both a rectifier unit for RF-DC conversion and an envelope detector unit for ASK signal demodulation to run in parallel. A power splitting technique is used to perform the simultaneous RF-DC conversion and signal demodulation. Using the splitting technique, a portion of the transmitted RF signal is sent along one branch of the circuit to be rectified for DC power while the rest is sent along the other branch to be demodulated through an envelope detector. In this chapter, the design of a simple, robust front-end receiver unit is introduced.

5.1 Rectifier Design

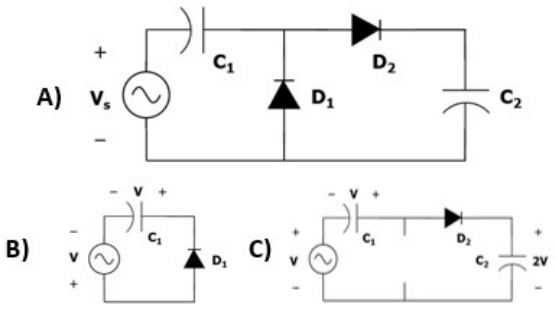

Figure 5.1 Schematics of (A) a voltage doubler, (B) the rectifier during negative half-cycle, and (C) the rectifier during positive half-cycle.

A rectifier is an electrical device that converts an AC power source into a DC power source through the use of diodes. One of the most fundamental types of a rectifier is the voltage doubler. As shown in Fig. 5.1a, the circuit consists of a voltage clamp and a peak detector. During the negative half-cycle of the signal, diode D_1 turns on and charges the capacitor up to the voltage equal to the amplitude of the signal-voltage across the diode (Fig. 5.1b). During positive half-cycle, the shunt diode is reverse biased and acts as an open circuit and the series diode D_2 conducts and charges the voltage of the capacitor C_2 to twice the signal amplitude by adding to the voltage from the first

capacitor to the signal voltage (Fig. 5.1c). Because the output is charged every half of the cycle, this voltage doubler is referred to as a half-wave voltage doubler.

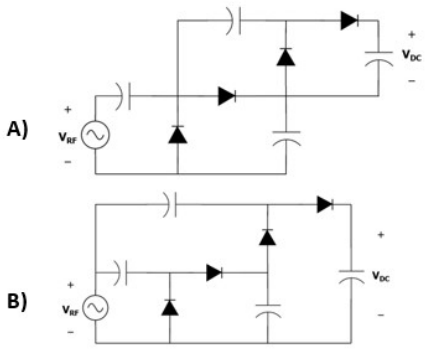

Figure 5.2 (A) Villard multiplier and (B) Dickson multiplier schematics.

Multiple voltage doublers can be cascaded to form a more complex rectifier, the voltage multiplier, which enhances the AC to DC conversion. As shown in Fig. 5.2, there are two basic types of the multiplier topologies: Villard and Dickson. Villard multiplier is a half-wave series multiplier, and the Dickson multiplier is a half-wave parallel multiplier [58]. For this device, because the Dickson multiplier requires less capacitance per stage than the Villard, it has more efficient use of space due to fewer capacitive lumped element components. Moreover, the parallel configuration of Dickson at each stage results in a lower input impedance, which is useful for impedance matching.

Since any voltage drop across the diode in the voltage doubler circuit will reduce the rectification efficiency of the system, diodes with the low turn-on voltages are used. Furthermore, due to the high frequency of the incoming signal, the diodes need to have a short switch time. One of the types of diode that can support a high-frequency signal is the Schottky diode which consists of a metal-semiconductor junction and has low equivalent resistance, low junction capacitance, and high saturation current. For this system, Avago HSMS-2852 Schottky diodes were selected for their low turn-on voltage of 150 mV and convenient packaging for voltage multiplier applications.

Since the topology and composition of the multipliers are known, the next step is to determine the optimum number of stages that will result in the best performance using simulation software.

5.2 Signal Demodulation

To support simultaneous power conversion and signal demodulation, the Dickson voltage multiplier must allow for power splitting. Power splitting is implemented by modifying a two-stage Dickson rectifier. The final rectifier design has been adopted from [59] as shown in Fig. 5.3.

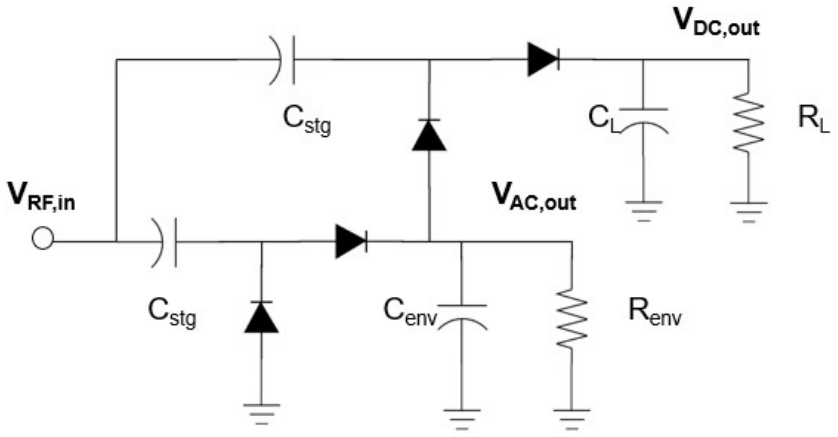

Figure 5.3 Rectifier and envelope detection circuit schematic.

The first stage of the rectifier builds up charge that is pumped to the second stage of the circuit and acts as an envelope detector for demodulation. The second stage of the rectifier performs the necessary RF-DC conversion that will be used to power the LCD device. The compact design of the circuit is desirable since it does not require separate rectification and demodulation circuits. The design shown in Fig. 5.3 is verified using the Harmonic Balance and Transient simulations in Keysight Advanced Digital System (ADS) software, with the simulation schematic shown in Fig. 5.4. The values of the lumped elements were optimized using ADS Tuning & Optimization to simultaneously maximize both the demodulation and the DC output.

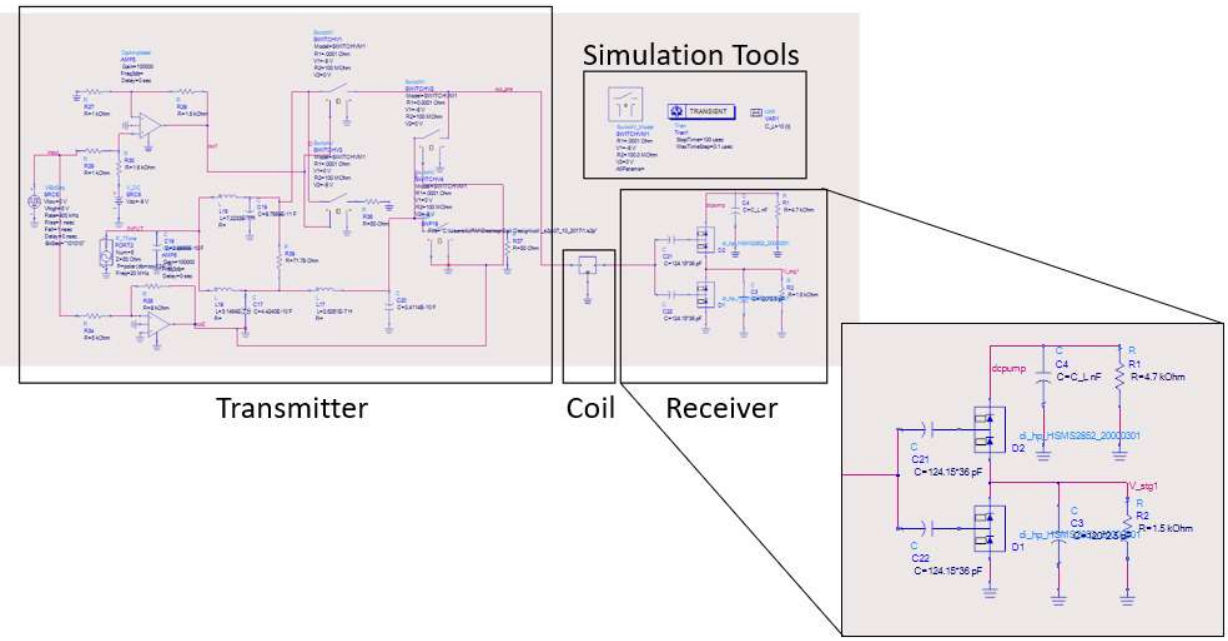

Figure 5.4 ADS schematic for the rectifier and envelope detection circuit.

The result of the transient simulation of the front-end receiver is shown in Fig. 5.5 and Fig. 5.6. The input RF signal is amplitude-shift key modulated with a modulation depth of 50% and contained a bit sequence of 1110 at a rate of 1 Mb/s. The average input power for this modulated signal can be found by using:

$$P_{avg} = \frac{N_H P_H + N_L P_L}{N_H + N_L} \tag{5.1}$$

where N_H, N_L, P_H, and P_L are the numbers of high and low states in the bit sequence, and the associated powers, respectively. For an average input power of 1 W, the designed receiver had a simulated PTE of 21.15% with small wake-up ramp time of 23 μsec. The low conversion efficiency is due to the power splitting technique used in the design. However, the output DC power is still enough to power the microdisplay and the processor which require less than 5 mW.

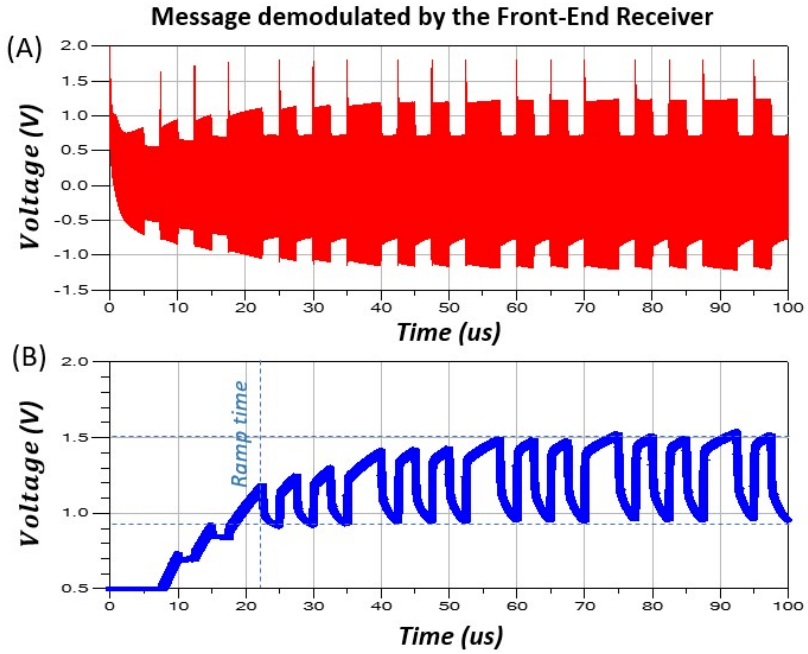

Figure 5.5 Transient analysis of the front-end receiver (A) modulated input signal and (B) demodulated signal with ramp time.

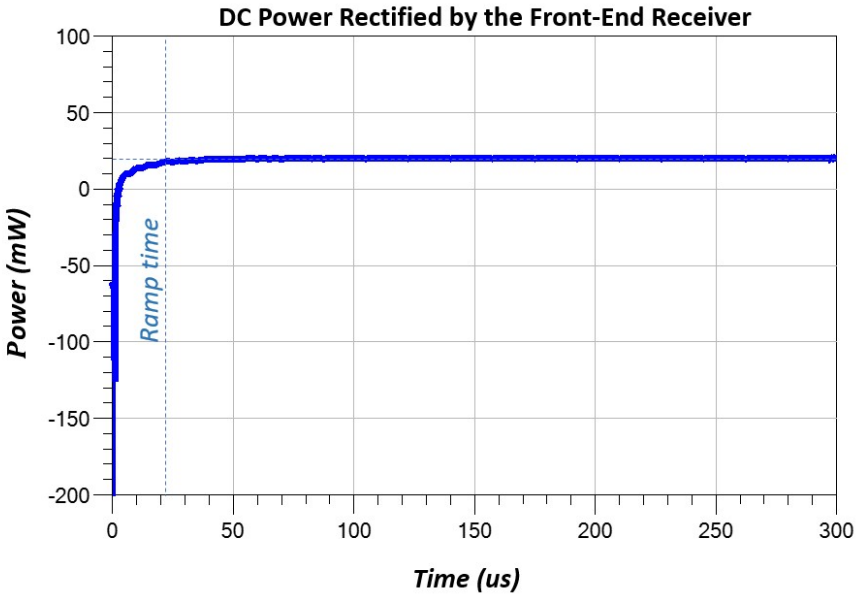

Figure 5.6 DC power ramp time required by the rectifier.

Chapter 6: Conclusion

6.1 Findings of this Work

This thesis has demonstrated the invention of a novel visual prosthetic using a wireless micro-projection device. Multiple commercially available components such as a micro-scale high resolution LED display, robust microprocessors, and resonant Qi-coils have been connected to achieve various proof of concept prototype designs. Through each generation of the prototype, parts of the device have been modified and improved upon to conform to the design constraints, in particular, the limited physical space of the inter-body regions and the allowed SAR threshold.

To overcome these obstacles and to inch closer to the ideal prototype of the device, a small, robust simultaneous power, and data transmission system was designed. Square spiral Tx and Rx antennas were designed and implemented on an LPKF® 1oz double-sided copper cladded FR4 board along with simultaneous matching network to improve the power transfer efficiency. In addition, a simple front-end receiver was designed to process rectification and demodulation in parallel by using the power splitting method.

Currently, animal testing is being performed at the University of Illinois Chicago Medical School using the third-generation PoC prototype as shown in Fig. 6.1.

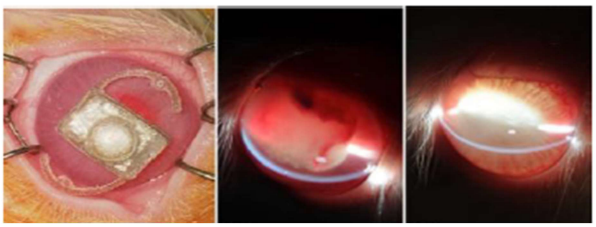

Figure 6.1. Rabbit study of the third-generation PoC prototype
(Courtesy of Prof. Charles Yu from Stanford University).

6.2 Future Work

There are several avenues for future research to increase the performance of the system and develop a fully working prototype of the intraocular prosthetic device. A few additional research areas are discussed here.

Integrating the front-end receiver with the video processor

Although this work successfully demodulated the signal from the ASK modulated input, the demodulated signal needs to be further processed and supply appropriate data to the video processor. The current prototype uses the Raspberry-Pi-Zero microcontroller to process the video data. However, the unit is too big to fit inside the body. A simple, robust DSP unit needs to be designed and implemented to be able to communicate with a video processor.

Improving the bandwidth of the dual-coil system

As seen in Chapter 4, the addition of a simultaneous conjugate matching network significantly increased the power transfer efficiency of the two coils. However, this was at the cost of a much narrower bandwidth which could result in an unreliable, ultra-sensitive network. The new approach should be further investigated to increase the bandwidth while maintaining high transfer efficiency.

Waterproofing of the receiver unit

Similar to the intraocular projector discussed in Chapter 4, the receiver unit will need to be waterproofed once the design is complete. The interior of the skull, being an immune-privileged space, is known to tolerate many materials well. The receiver housing can be made up of MED610 material, like that of the intraocular display. MED610 materials have been tested for biocompatibility by the International Organization for Standardization (ISO) 10993-1.

References

[1] R. Sharma, "Why eye is the important sensory organ in our Life?," *InsysdNet*, p. 12, May-2017.

[2] H. C. Ørsted, *Selected Scientific Works of Hans Christian Orsted*. Princeton University Press, 1998.

[3] S. Y. R. Hui, W. Zhong, and C. K. Lee, "A critical review of recent progress in mid-range wireless power transfer," in *IEEE Transactions on Power Electronics*, vol. 9, pp. 4500-4511, 2014.

[4] "Inventions & experiments of Nikola Tesla." [Online]. Available: https://teslaresearch.jimdo.com/.

[5] A. I. Al-Kalbani, M. R. Yuce, and J. M. Redoute, "A biosafety comparison between capacitive and inductive coupling in biomedical implants," in *IEEE Antennas Wirel. Propag. Lett.*, vol. 13, pp. 1168-1171, 2014.

[6] S. K. S. Gupta, S. Lalwani, Y. Prakash, E. Elsharawy, and L. Schwiebert, "Towards a propagation model for wireless biomedical applications," in *2003 IEEE International Conference on Communications* -, pp. 1993-1997, 2003.

[7] M. Jawad, A. Nordin, R. Gharghan, S. Jawad, and H. Ismail, "Opportunities and challenges for near-field wireless power transfer: a review," *Energies*, vol. 10, no. 1022, pp. 7, 2017.

[8] "Wireless infrastructure market size worth $116.75 billion by 2025," *Grand View Research*, 2018. [Online]. Available: https://www.grandviewresearch.com/press-release/global-wireless-infrastructure-market.

[9] R. L. Abboudi, C. A. Glass, N. A. Newby, J. A. Flint, and W. Craelius, "A biomimetic controller for a multifinger prosthesis," in *IEEE Trans. Rehabil. Eng.*, vol. 7, no. 2, pp. 121-129, 1999.

[10] "Why good vision is so important," *Zeiss*, 2017. [Online]. Available: https://www.zeiss.com/vision-care/int/better-vision/health-prevention/why-good-vision-is-so-important-.html.

[11] World Health Organisation, "Visual impairment and blindness (Fact Sheet N°282)," www.who.int, 2013.

[12] "Corneal blindness." [Online]. Available: https://www.seeintl.org/corneal-blindness/,2018.

[13] "Function of the cornea," *Massachusetts Eye and Ear*, 2018. [Online]. Available: https://www.masseyeandear.org/for-patients/patient-guide/patient-education/diseases-and-conditions/cornea/function.

[14] P. Gain *et al.*, "Global survey of corneal transplantation and eye banking," *JAMA Ophthalmol.*, vol. 134, pp. 167-173, 2016.

[15] H. F. Chew *et al.*, “Boston Keratoprosthesis outcomes and complications,” *Cornea*, 2009.

[16] L. da Cruz *et al.*, “Five-year safety and performance results from the Argus II retinal prosthesis system clinical trial,” *Ophthalmology*, vol. 123, no. 10, pp. 2248-2254, 2016.

[17] K. Stingl *et al.*, “Artificial vision with wirelessly powered subretinal electronic implant alpha-IMS,” *Proc. R. Soc. B Biol. Sci.*, vol. 280, pg. 1757, 2013.

[18] J. H. Tsai, E. Derby, E. J. Holland, and A. K. Khatana, “Incidence and prevalence of glaucoma in severe ocular surface disease,” *Cornea*, vol.25, pp. 530-532, 2006.

[19] “Posterior chamber of eye diagram.” [Online]. Available: http://radkan.co/posterior-chamber-of-eye-diagram.html.

[20] C. E. Willoughby, D. Ponzin, S. Ferrari, A. Lobo, K. Landau, and Y. Omidi, “Anatomy and physiology of the human eye: Effects of mucopolysaccharidoses disease on structure and function - a review,” *Clinical and Experimental Ophthalmology*, vol. 38, pp. 2-11, 2010.

[21] P. L. Turner and M. A. Mainster, “Circadian photoreception: Ageing and the eye’s important role in systemic health,” *British Journal of Ophthalmology*, vol. 89, pp. 1439-1444, 2008.

[22] C. S. McCaa, “The eye and visual nervous system: anatomy, physiology and toxicology,” *Environ. Health Perspect.*, vol. 44, pp. 1-8, 1982.

[23] P. Artal, “The eye as an optical instrument,” in *Optics in Our Time*, 2016, pp. 285-297,.

[24] R. Spector, *Clinical Methods: The History, Physical, and Laboratory Examinations*, Third. Butterworth-Heinemann, 1990.

[25] I. Bekerman, P. Gottlieb, and M. Vaiman, “Variations in eyeball diameters of the healthy adults,” *J. Ophthalmol.*, pp. 1-5, 2014.

[26] P. Artal, “Image formation in the living human eye,” *Annu. Rev. Vis. Sci.*, pp. 1-17, 2015.

[27] O. J. Gomez Diaz and M. D. Cruz Sanchez, “Anatomical and clinical study of the posterior auricular artery angiosome: In search of a rescue tool for ear reconstruction,” *Plast Reconstr Surg Glob Open*, vol. 4, pp. 1-12, 2016.

[28] ICT Data and Statistics Division, “ICT facts and figures,” 2016.

[29] International Commission on Non-Ionizing Radiation Protection, "ICNIRP guidelines for limiting exposure to time-varying electric and magnetic fields (1 Hz - 100 kHz)," published in *Health Physics*, vol. 99, no. 6, pp. 818-836, 2010 .

[30] Y. Touitou and B. Selmaoui, “The effects of extremely low-frequency magnetic fields on melatonin and cortisol, two marker rhythms of the circadian system,” *Dialogues Clin. Neurosci.*, vol. 14, no.4, pp. 381-399, 2012.

[31] National Research Council (US) Committee on Assessment of the Possible Health Effects of Ground Wave Emergency Network (GWEN), “Effects of electromagnetic fields on organs and tissues,” *Natl. Acad. Press*, vol. 6, pp. 1-182, 1993.

[32] "Science Lesson: An introduction to remote sensing," *The Weather Club: Royal Meteorological Society*, pp. 7, 2016.

[33] J. C. Lin, "Cataracts and cell-phone radiation," *IEEE Antennas Propag. Mag.*, vol. 45, pp.171-174, 2003.

[34] J. A. Elder, "Ocular effects of radiofrequency energy," in *Bioelectromagnetics*, vol. 6, pp. 148-161, 2003.

[35] K. Classic, "Radiofrequency (RF) radiation," *Health Physics Society*. [Online]. Available: https://hps.org/hpspublications/articles/rfradiation.html.

[36] H. I. Atasoy, M. Y. Gunal, P. Atasoy, S. Elgun, and G. Bugdayci, "Immunohistopathologic demonstration of deleterious effects on growing rat testes of radiofrequency waves emitted from conventional Wi-Fi devices," *J. Pediatr. Urol.*, vol. 9, no. 2, pp. 223-229, 2013.

[37] A. Özorak *et al.*, "Wi-Fi (2.45 GHz)- and mobile phone (900 and 1800 MHz)-Induced risks on oxidative stress and elements in kidney and testis of rats during pregnancy and the development of offspring," *Biol. Trace Elem. Res.*, vol. 156, pp. 221-229, 2013.

[38] G. Aynali, M. Naziroğlu, Ö. Çelik, M. Doğan, M. Yariktaş, and H. Yasan, "Modulation of wireless (2.45 GHz)-induced oxidative toxicity in laryngotracheal mucosa of rat by melatonin," *Eur. Arch. Oto-Rhino-Laryngology*, vol. 270, pp. 1695-1700, 2013.

[39] Z. Z. Çiftçi, Z. Kırzıoğlu, M. Nazıroğlu, and Ö. Özmen, "Effects of prenatal and postnatal exposure of Wi-Fi on development of teeth and changes in teeth element concentration in rats: Wi-Fi (2.45 GHz) and teeth element concentrations," *Biol. Trace Elem. Res.*, vol. 163, pp. 193-201, 2015.

[40] M. Nazıroğlu, M. Kahya, Ö. Tök, S. Doğan, and L. Tök, "Effects of melatonin on Wi-Fi-induced oxidative stress in lens of rats," *Indian J. Ophthalmol.*, vol. 62, pp. 12-15, 2014.

[41] World Health Organization, "IARC classifies radiofrequency electromagnetic fields as possibly carcinogenic to humans," *Int. Agency Res. Cancer,*, 2011.

[42] IEEE Standards Coordinating Committee 28, *IEEE C95. 1-1992: IEEE Standard for Safety Levels with Respect to Human Exposure to Radio Frequency Electromagnetic Fields, 3 kHz to 300 GHz*. 1999.

[43] Sony Corporation, "Sony releases 0.5-type OLED microdisplay with top-of-class UXGA resolution, featuring the world's smallest pixel pitch of 6.3µm," *Sony Semiconductor Solutions Corporation*, 2018. [Online]. Available: https://www.sony.net/SonyInfo/News/Press/201805/18-049E/index.html.

[44] E. Wageningen, Dries Waffenschmidt, "Transfer efficiency," *Wireless Power Consortium*. [Online]. Available: https://www.wirelesspowerconsortium.com/technology/transfer-efficiency.html.

[45] D. Pozar, *Microwave Engineering*, 4th ed. Wiley, 2009.

[46] W. H. Ko, S. P. Liang, and C. D. F. Fung, "Design of radio-frequency powered coils for implant instruments," *Med. Biol. Eng. Comput.*, 1977.

[47] N. de N. Donaldson and T. A. Perkins, "Analysis of resonant coupled coils in the design of radio frequency transcutaneous links," *Med. Biol. Eng. Comput.*, vol. 15, pp. 634-640, 1983.

[48] C. M. Zierhofer and E. S. Hochmair, "High-efficiency coupling-insensitive transcutaneous power and data transmission via an inductive link," *IEEE Trans. Biomed. Eng.*, vol.7, pp. 716-722, 1990.

[49] C. M. Zierhofer and E. S. Hochmair, "Geometric approach for coupling enhancement of magnetically coupled coils," *IEEE Trans. Biomed. Eng.*, vol. 43, pp. 708-714, 1996.

[50] W. J. Heetderks, "RF powering of millimeter- and submillimeter-sized neural prosthetic implants," *IEEE Trans. Biomed. Eng.*, vol. 35, pp. 323-327, 1988.

[51] Z. Yang, W. Liu, and E. Basham, "Inductor modeling in wireless links for implantable electronics," *IEEE Trans. Magn.*, vol. 5, pp. 579-591, 2007.

[52] S. S. Mohan, M. D. M. Hershenson, S. P. Boyd, and T. H. Lee, "Simple accurate expressions for planar spiral inductances," *IEEE J. Solid-State Circuits*, vol. 26, pp. 6040, 1999.

[53] M. Soma, D. C. Galbraith, and R. L. White, "Radio-Frequency codes in implantable devices: misalignment analysis and design procedure," *IEEE Trans. Biomed. Eng.*, vol. 34, pp. 276-282, 1987.

[54] U. M. Jow and M. Ghovanloo, "Design and optimization of printed spiral coils for efficient inductive power transmission," in *Proceedings of the IEEE International Conference on Electronics, Circuits, and Systems*, pp. 70-73, 2007.

[55] M. W. Baker and R. Sarpeshkar, "Feedback analysis and design of RF power links for low-power bionic systems," *IEEE Trans. Biomed. Circuits Syst.*, vol. 1, pp. 28-38, 2007.

[56] S. Gabriel, R. W. Lau, and C. Gabriel, "The dielectric properties of biological tissues: II. Measurements in the frequency range 10 Hz to 20 GHz," *Phys. Med. Biol.*, vol. 41, pp. 2251-2269, 1996.

[57] J. M. Kim *et al.*, "In vitro and in vivo measurement for biological applications using micromachined probe," in *IEEE Transactions on Microwave Theory and Techniques*, pp. 2918-2923, 2005.

[58] P. Nintanavongsa, U. Muncuk, D. R. Lewis, and K. R. Chowdhury, "Design optimization and implementation for RF energy harvesting circuits," *IEEE J. Emerg. Sel. Top. Circuits Syst.*, vol. 2, pp. 24-33, 2012.

[59] B. Arakawa *et al.*, "Simultaneous wireless power transfer and communication to chip-scale devices," in *IEEE MTT-S International Microwave Symposium Digest*, pp. 311-314, 2017.

[60] N. Kuo and A. M. Niknejad, "Single-Antenna FDD Reader Design and Communication to a Commercial UHF RFID Tag," in *IEEE Microwave and Wireless Components Letters*, vol. 28, no. 7, pp. 630-632, July 2018.

[61] N. Kuo and A. M. Niknejad, "Single-Antenna FDD Reader Design and Communication to a Commercial UHF RFID Tag," in *IEEE Microwave and Wireless Components Letters*, vol. 28, no. 7, pp. 630-632, July 2018.

[62] Liuqing Gao, Yansong Yang, A. Brandon, J. Postma and Songbin Gong, "Radio frequency wireless power transfer to chip-scale apparatuses," *2016 IEEE MTT-S International Microwave Symposium (IMS)*, San Francisco, CA, 2016, pp. 1-4.